Lateritic weathering of trachyte, and bauxite formation in West Cameroon : Morphological and geochemical evolution

Mathieu Nouazi Momo, Anicet Beauvais, Paul Tematio, Jean-Paul Ambrosi, Martin Yemefack, Bernard Palmer Kfuban Yerima, Rose Yongue-Fouateu

Lateritic weathering of trachyte, bauxite formation in West Cameroon: Morphological and geochemical evolution

Mathieu Momo Nouazi Momo*[1], Anicet Beauvais[2], Paul Tematio[3], Jean-Paul Ambrosi[2], Martin Yemefack[4], Bernard Palmer Kfuban Yerima[5], Rose Yongue-Fouateu[6]

[1]Institute of Geological and Mining Research (IRGM), P.O. Box 4110 Yaoundé, Cameroon

[2]Aix-Marseille Univ, CNRS, IRD, Coll France, CEREGE, BP 80, 13545, Aix-en-Provence, Cedex 4, France

[3]University of Dschang, Faculty of Science - Department of Earth Sciences. P.O. Box 67 Dschang - Cameroon

[4]International Institute of Tropical Agriculture (IITA), ASB Partnership REALU Project, P.O. Box 2008 (Messa) Yaoundé, Cameroon

[5]University of Dschang, Faculty of Agronomy and Agricultural Research, P.O. Box 222 Dschang, Cameroon

[6]University of Yaoundé 1, Faculty of Science, Department of Earth Sciences. P.O. Box 337 Yaoundé, Cameroon

Journal of Geochemical Exploration, 205, (2019) 106324

*Corresponding author Email: nouazimat@yahoo.fr

Abstract

Bauxites and Fe laterites were formed on Neogene volcanics from Fongo-Tongo region in the highlands of western Cameroon, and are distributed on plateaus, slopes and downslope surfaces. Bauxitic profiles result from intense in-situ weathering of trachytes that implied depletion of silica and labile elements from the saprolite, while alumina relatively accumulated from parent minerals pseudomorphosis by primary gibbsite formation. During ongoing lateritization and bauxite maturation, important leaching and illuviation processes resulted in secondary gibbsite crystallizations. Late incision and dissection of upper bauxitic plateau resulted in degradation and dismantling of bauxitic duricrusts with Fe-depletion and increasing silica. Compared to trachyte, bauxitic duricrusts are relatively enriched in Nb, Zr, Ga, Ni, Cu, Co, V, Cr, As, Pb, Th, Hf, U and Ta, while Y, Sr, Rb, Ba and Zn are depleted. Trace elements contents depend on relative proportions of gibbsite, kaolinite, iron oxides and anatase and their affinity with these minerals across the weathering sequence. The overall REE composition and C1-Chondrite normalized REE patterns highlight significant fractionations with enrichment in the upslope profile and labile behavior in other profiles of the sequence. Our results document two major bauxitic phases in the Fongo-Tongo area, i.e., mid-Miocene primary in situ bauxitic weathering of trachyte and late Miocene secondary bauxitization of previously formed bauxitic profiles that led to alumina enrichment up to 53.50 wt.%. Combined together, the morphological distribution and geochemical composition of the studied bauxitic profiles constitute guides for bauxite exploration, and more generally document the dynamics and morphogenetic evolution of lateritic landforms in West Cameroon.

Keywords: Bauxite, Lateritic weathering, Gibbsite, Rare Earth Elements, Neogene, Cameroon

47 # 1. Introduction

48 The African tropical belt hosts the most widespread lateritic landforms on the earth
49 surface from West to Central Africa (Tardy, 1997). These landforms expose unconsolidated
50 materials from basement rock to groundsurface resulting from lateritic weathering of a variety
51 of parent materials. As so, tens of meters' thick regolith mantles were formed, and are
52 relatively well preserved despite obvious landscape dissection (Grandin, 1976; Tardy and
53 Roquin, 1998; Taylor and Howard, 1998; Taylor and Eggleton, 2001). The morphological
54 structure of these lateritic surfaces, and mineralogical / geochemical features of their
55 weathering soils and profiles reflect long and complex evolutions during successive
56 morphoclimatic and geochemical changes over time (Nahon, 1986; Tardy, 1997).

57 Past and recent studies of lateritic geosystems in West Africa emphasized their
58 geomorphological distribution at various spatial and temporal scales (e.g., Beauvais and
59 Chardon, 2013; Beauvais and Roquin, 1996; Grimaud et al., 2015); and their genetic and
60 evolution processes were described in Central Africa (Beauvais, 1999, 2009). Particular
61 interest was also devoted to relict lateritic terrains of economic potential, formed by intense
62 chemical rock weathering under warm and humid climates that has led to accumulation of
63 metals among which Al, Fe, Mn, Ni, Cu, Cr, Ag, and Pt, and exportation of soluble elements
64 (Boulangé et al, 1997; Colin et al., 2004; Nahon, 1991; Tardy, 1997; Traore et al., 2008a-b).
65 Most of these studies focused on steady cratonic landscapes (e.g., West Africa), but few
66 studies have described the petrologic and geomorphic features of lateritic landsurfaces and
67 associated regolith in epirogenic area such as that of the Western highlands in Cameroon (Fig.
68 1a). In this region, widespread lateritic landsurfaces bear various lateritic weathering mantles
69 upon various lithologies, and under different climatic and tectonic regimes. A unique
70 geormorphic sequence exhibits highly elevated bauxitic surfaces up to ca. 1900 m on

71 successive Neogene volcanics, stepped with wide relicts of Fe-duricrusted surfaces (Momo
72 Nouazi, 2016). In this environment, issues aimed mainly at providing geochemical and
73 mineralogical data useful for bauxite exploration given the renewed interest in mineral
74 resource assessment and inventory for this developing country (Cameroon Alumina LTD.,
75 2008; Momo Nouazi et al., 2016; Tematio et al., 2015). Few studies were devoted to the
76 description and quantification of weathering processes of these bauxitic landsurfaces for
77 highlighting the influence of combined lithotectonic and morphoclimatic factors. We describe
78 the morphological, mineralogical and geochemical features of the lateritic weathering and
79 bauxites developed on trachytes in the Fongo-Tongo area (West Cameroon; Fig. 1b), and we
80 derive chemical indices of alteration and intensity of lateritization that document all together
81 the formation and evolution processes of lateritic soil profiles and their bauxitization.
82

83 2. Morphogeological setting of the study area

84 The Fongo-Tongo laterites formed upon the so-called “upper lateritic surface” of the
85 Bamiléké plateau, which is part of the Western Cameroon highland located at 05°10’ to
86 05°56’N and 09°44’ to 10°33’E, between the Bamoun plateau in the east, the Grassfields in
87 the north and the Mbô plain in the southwest (Fig. 1a and 1b). It covers a surface of ~ 4.52
88 km² between altitudes of 1580 m to ca. 1900 m on the southern flank of the Bambouto
89 volcano (Momo Nouazi et al., 2016), which is the main morphogeological feature of the
90 Bamiléké plateau culminating at the altitude of 2740 m (Fig. 1b), and the third most important
91 volcano of the Cameroon Volcanic Line (Déruelle et al., 1991). The region is subjected to a
92 sub-equatorial climate, which is influenced by high altitudes (1500 to ≥ 2500 m) with ca.
93 1600 mm mean annual rainfall and ca. 18°C for the mean annual temperature (Kengni et al.,
94 2009).

The Cameroon Volcanic Line includes wide Cenozoic volcanic complexes and mafic and felsic plutons extruded through the Neoproterozoic granito-gneissic basement (Kwekam et al., 2010). The volcanic complex of the Bamiléké plateau is made up mainly of basalts, trachytes and ignimbrites (Fig. 1c). The ^{40}K-^{40}Ar geochronological data suggested three main periods of volcanic activity extending from the Miocene (ca. 19 Ma, Burdigalian) (Nkouathio et al., 2008) up to ca. 0.5 Ma with uncommon lava flows (Kagou Dongmo et al., 2010). These periods refer to (i) the pre-caldera magmatism characterized by fissure-related basalts of strombolian activity (Nono et al., 2004), (ii) the caldera formed by eruption (Burdigalian to Tortonian, 18.1±0.01 Ma to 11.1±0.02 Ma) with pyroclastic rocks as trachytes and scarce rhyolites (Nkouathio et al., 2006), and (iii) the post-caldera extrusive domes from 7.75±0.01 Ma to 4.52±0.28 Ma and late quaternary basalts flow at 0.480 ± 0.014 Ma (Kagou Dongmo et al., 2010).

Bauxites formed upon trachytes are preserved in the southern part of the Bambouto volcano (Fig. 1b), which erupted at 16±0.39 Ma (Nkouathio et al., 2006). Massif outcrops of trachytes occur on slope and in talwegs. These rocks are made up essentially of a microlithic assemblage of plagioclases (Pl), clinopyroxenes (cpx), Fe-Ti oxides, and scarce Pl and cpx phenocrysts (up to 1 mm; Fig. 1d and 1e). According to Nkouathio et al. (2008), these minerals include anorthoclase ($An_{25–11}\,Ab_{70–54}\,Or_{22–19}$) and alkali feldspar, i.e., sanidine to Na-sanidine ($Or_{15–55}Ab_{35–85}An_{0–6}$), sodic cpx ($En_{3–4}Aeg_{33–35}Fs_{62–65}$) or hedenbergite ($Wo_{45–47}En_{26–30}Fs_{40–44}$) and titanomagnetite (94-25 mol% ulvöspinel). The chemical composition of trachytes comprises 58.74 to 62.73 wt.% SiO_2, 14.26 to 18.84 wt.% Al_2O_3, 5.11 to 6.55 wt.% Fe_2O_3, 5 to 5.44 wt.% Na_2O, and 2.99 to 5.58 wt.% K_2O (Nkouathio et al., 2008).

3. Materials and methods

We implemented detailed morphological description, X-ray Diffraction (XRD), ICP geochemistry, and we calculated chemical indices of weathering and lateritization to document the formation and evolution of the lateritic bauxitic profiles along a 300 m long topographical sequence. Four pits were bored through thick lateritic mantle, which depth reaches 6 to 12 m, respectively on the plateau (P1-FO), upslope (P2-FO), hillslope (P3-FO) and downslope (P4-FO) (Fig. 2a). These profiles exhibit various petrographic horizons. The lateral weathering sequence was reconstructed based on profile description including macro-morphological description of petrographic structures using the reference works of Nahon (1991) and Tardy (1997). Thirty-four samples were collected along each profile and prepared for micro-morphological observations, mineralogical and geochemical analysis. Polished thin sections of undisturbed collected samples were observed under optical microscope and described according to reference terms defined by Brewer and Sleeman (1988).

All samples were sorted and ground to produce powders with a sieve size < 63 μm, which were analyzed by XRD, using an X'Pert PANalytical diffractometer with CuKα radiation (1.79 Å) in the range of 2° to 78° 2θ and at a speed of 0.2°/min (0.033° for 10s counting time). Minerals were identified upon diffraction spectra using High Score X'Pert Plus software (Version 3.0) and compared with known standards (American Mineralogist Crystal Structure Database, 2016). A Rietveld Refinement process (Rietveld, 1969; Ufer et al., 2008) was also applied for semi-quantifying the proportion (%) of each mineral. Each Mineral proportion is obtained by the ratio between the surface areas of specific XRD peaks of each mineral to the total surface of the sample XRD pattern.

Geochemical analyses were obtained using ICP methods from pulverized samples fraction of the samples. Major and trace elements were analyzed by ICP-AES (Inductively

coupled plasma-Atomic emission spectrometry), while rare earth elements (REE) were analyzed by ICP-MS (Inductively coupled plasma-Mass spectrometry). The resulting geochemical data were interpreted and discussed for highlighting the behavior of major elements, trace elements and REE during trachyte weathering that document key weathering factors.

The geochemical indices were calculated for better understanding and quantifying processes of weathering, bauxitization and late bauxite degradation/dismantling. The Chemical Index of Alteration (CIA), and the Mafic Index of Alteration (MIA) were used to quantify both mafic and felsic mineral components of rock weathering (Nesbit and Young, 1982; Babechuck et al., 2014). These indices are expressed as molecular ratios between mobile and immobile elements, and are thus suitable to define the weathering intensity (Durgoren-Aydin, 2002). The CIA was used to describe feldspar dissolution and the concomitant release of Ca, Na, and K relative to Al during the weathering. According to this approach:

$$CIA\ (\%) = 100 \times Al_2O_3/(Al_2O_3+CaO^*+Na_2O+K_2O) \quad (1)$$

CaO* being the amount of CaO incorporated in the silicate fraction of fresh rock.

The MIA includes Mg and Fe, thereby allowing characterization of weathering of mafic minerals as pyroxenes according to the formula:

$$MIA=100 \times (Al_2O_3+Fe_2O_3)/(Al_2O_3+Fe_2O_3+MgO+CaO^*+NaO+K_2O) \quad (2)$$

The Ki ratio ($Ki=SiO_2/Al2O_3$) was also calculated to estimate the degree of chemical weathering of volcanic rocks (Irfan, 1999).

Finally, the different stages of chemical weathering were determined by the Index Of Lateritization (IOL), which considers the main major elements (Al-Si-Fe) involved in the

dominant processes and the resulting residue. The IOL was estimated according to a method used by Babechuck et al. (2014), i.e.:

$$IOL = 100 \times (Al_2O_3+Fe_2O_3)/ (SiO_2+Al_2O_3+Fe_2O) \quad (3)$$

The computed IOL values are reported along with a ternary diagram (SiO_2-Al_2O_3-Fe_2O_3) for classification into kaolinized, weakly lateritized, moderately lateritized and strongly lateritized ferritic or bauxitic horizons (Schellmann, 1994).

4. Results and Discussion

Field observations and morphological descriptions along the sequence of pits across two geomorphological segments (Fig. 2a) revealed six different weathering horizons. From bottom to top of profiles, we have identified and described a saprolite (C), a blocky bauxitic duricrust (B13), a massive bauxitic duricrust (B12) and a nodular bauxitic horizon (B11; see Fig. 3a) on the plateau; and, a bauxitic pebbly duricrust (B15), and a fine earthy horizon (B14) in downslope profile (Figs. 2a, 2b). In this section, detailed petrological descriptions of weathering horizons highlights vertical and lateral morphologic changes along the sequence with reference to Fig. 3 and Fig. 4. Based on these descriptions, mineralogical and geochemical variations along a composite upslope profile (P2-FO and saprolite of P3-FO) document major patterns of lateritic bauxite evolution.

4.1. Major petrological features across the weathering profiles sequence

On the plateau, the saprolite (horizon C) overlying the parent rock is highly porous and composed of a greyish matrix with reddish to dark micrometric features preserving the porphyry structure of the trachyte. The blocky bauxite duricrust (B13) overlying the saprolite (Fig. 2a and 2b) includes decimetric blocks of porous reddish bauxitic duricrust mixed with centimetric coarse nodules and loose matrix. It is overlained by a yellowish saprolite-like

duricrusted matrix crossed by sub-horizontal centimeter size massive dark and elongated domains (Fig. 3b), marking the transition with the uppermost horizons. The massive bauxitic duricrust (B12; Fig. 2a and 2b) is made up of a reddish to yellow brown matrix with interconnected voids coated by 1 to 2 mm thick yellowish cutans (Fig. 3c); higher in the horizon B12, the voids are filled with a crumbly reddish matrix (Fig. 3d). The surface horizon (B11) is continuous on the plateau (Fig. 3a); it is made up of a loose matrix embedding fragments of bauxitic duricrust and bauxitic nodules whose petrographic structure is quite similar to that of underlying massive bauxite.

The bauxitic pebbly duricrust of the downslope profile (B15; Figs. 2a and 2b) is made up of a reddish massive matrix cementing coarse duricrust pebbles with compact and massive internal structure; voids of the matrix are filled by red to yellowish loose fine earth (Fig. 3e). The heterogeneous structure of this horizon is suggestive of allochthonous materials, possibly imported from erosion of the uppermost lateritic plateau. The loose fine earth layer (B14) over the bauxitic pebbly duricrust is dark red and highly porous.

Under the microscope, saprolite is made up of two different weathering plasmas crossed by interconnected micrometer to millimeter-sized voids (Fig. 4a). Feldspars (mostly plagioclases) are weathered and replaced by grey brown crystic plasma composed of in-situ formed primary gibbsite and some relicts of clinopyroxene phenocrysts (Fig. 4a). The gibbsitic plasma is surrounded by grey argillic plasma with preserved trachytic features (Fig. 4a). Both mineralogical composition (See Fig. 5) and Rietveld refinement semi-quantification from XRD (hillside profile, P3-FO; Tab. 1) highlight the predominance of kaolinite (61%), gibbsite (16%), and goethite (7%). Anatase (8%) and maghemite (5%) are also identified (Fig. 6a and Tab. 1) with traces of florencite (Fig. 5c).

In the blocky bauxitic duricrust (B14), the microstructure of coarse features (bauxitic blocks and nodules) exhibits a predominance of reddish brown argillic plasma (Fig. 4b), probably made up of kaolinite coated with goethite; and a preservation of trachytic structure with clinopyroxene phenocrysts and dark micrometric anatase and maghemite. This plasma is also crossed by cracks filled with secondary gibbsite (Fig.4b). The mineral composition (Fig. 5 and Tab. 1) indicates up to 56% of kaolinite in the loose matrix, which is close to the content of the underlying saprolite (P3-FO; Tab. 1). A decreasing trend with 16% in the bauxitic nodules and lowest content (< 5%) in the massive bauxitic blocks is noticed in the upslope profile (P2-FO) (Fig. 6a and Tab. 1). Gibbsite and goethite varies from 23% and 8% in the loose matrix, to 57% and 29% in bauxitic blocks, respectively (Tab. 1).

The yellowish matrix at the bottom of the massive bauxite duricrust has a saprolite-like structure with grey argillic weathering plasma (Fig. 4c), composed of up to 68% gibbsite and 33% goethite (Tab. 1), and is locally preserved upward in the massive bauxite. The microstructure of the surrounding massive dark domains is made up of a dark brown argilic weathering plasma crossed by millimeter size interconnected cracks filled with secondary gibbsite crystals (Fig. 4d) resulting in 58% of goethite, 40% of gibbsite and up to 13% hematite (P2-FO; Tab. 1).

The micro-morphological organization of the massive bauxite duricrust (B12) is quite similar to that of the blocky bauxitic horizon and reveals abundant secondary gibbsite differentiated from the reddish-brown weathering plasma and thick clay Fe-rich cutans in interconnected voids (Fig. 4e); the secondary gibbsite crystals filling voids may derive from congruent dissolution of cpx (Fig. 4f). The resulting mineralogical composition along the plateau profiles (Fig. 5 and Tab. 1) highlights up to 66% of gibbsite, increasing content of goethite from 21% to 31% (Fig.6a, and Tab. 1), and hematite content less than 9% despite

236 local enrichment up to 22% on P1-FO profile (Tab. 1). The microstructure of cutans is
237 composed of yellow brown argilic plasma of kaolinite and goethite, and also secondary
238 crystals of gibbsite as “gibbsitans” (Fig. 4e) (Boulangé, 1984; Soares de Oliveira et al., 2013).
239 Noticed that traces of florencite are detected in some XRD diagrams (ex: P2-FO.5, Fig. 5b).

240 In the surface nodular horizon (B11), the internal structure of coarse bauxitic
241 fragments and nodules is similar to that of the underlying massive bauxite suggesting
242 inheritance from this fragmented duricrust. The mineralogical composition displays an
243 increasing trend from the lowest kaolinite content in the massive bauxitic blocks (< 5%), to
244 9% in the loose matrix as shown in the upslope profile (Fig. 6a and Tab. 1), and a maximum
245 of 22% on top of the hillside profile (P3-FO; Tab. 1). A decreasing trend is noticed for
246 gibbsite and goethite with 65% to 43% and 25% to 23%, in the massive blocks and the loose
247 matrix, respectively (Fig. 6a and Tab. 1). A quartz amount up to 17% is also measured in the
248 loose matrix.

249 In the downslope profile, in addition to the heterogeneous and polygenic structures of
250 the horizons, other dissimilarities with the plateau profiles include higher proportions of
251 kaolinite up to 28% in the porous duricrusted matrix and lesser goethite with a minimum of
252 7% with ca. 60 % gibbsite (Fig. 5d; Tab. 1). The coarse bauxitic pebbles clearly differentiates
253 from the surrounding matrix with maximum gibbsite content (71%), lowest kaolinite content
254 (7%), and highest goethite content (16%) suggesting that these duricrusted pebbles may be
255 inherited from massive bauxites of the plateau. Finally, the loose fine earth at the surface has
256 a mineralogical composition similar to that of the surface nodular horizon (B11) of the plateau
257 profiles, with quartz content of 13% (Tab.1).

258 **4.2. Geochemical differentiations across the weathering profiles sequence**

259 Major elements contents and chemical weathering indices are given in table 2, and
260 their typical vertical changes are displayed in the composite profile of the plateau including
261 the profile P2-FO and the saprolite of P3-FO (Fig. 6b and 6c). The chemical composition of
262 the saprolite C (Fig. 6b) shows a decreasing SiO_2 content (26.40 wt.%) and increasing Al_2O_3
263 (34.30 wt.%), Fe_2O_3 (17.30 wt.%) and TiO_2 (3.33 wt.%) relative to trachyte. At this stage, the
264 Ki ratio of 0.77 against 3.84 for the trachyte highlights Al_2O_3 enrichment relative to SiO_2
265 (Tab. 2). The CIA value of 86.8% (Fig. 6c and Tab. 2), attests to strong export of mobile
266 elements (Ca, Na, and K) consequently to intense feldspar pseudomorphic alteration mostly
267 into kaolinite, and gibbsite in a lesser measure. The MIA value of 91.7% compared to 53.1%
268 in the trachyte further indicates intense dissolution of cpx and consecutive Mg removal. The
269 calculated IOL value of 66.1% for the saprolite (Fig. 6c and Tab. 2) against 28.7% for the
270 trachyte indicates a weak lateritization (Fig. 7) during the first stage of bauxitization.

271 The geochemical composition of the blocky bauxitic duricrust (B13) is marked by
272 maximum SiO_2 content (19.50 wt.%) measured in the loose matrix of P3-FO profile (Tab. 2),
273 while minimum content of 1.59 wt.% is noticed in the massive bauxitic blocks of P2-FO
274 profile (Fig. 6b and Tab. 2). An increasing trend is noticed for Al_2O_3 contents from 35.50
275 wt.% in the loose matrix of the blocky bauxitic duricrust in the P3-FO profile, to 49.40 wt.%
276 in the massive bauxitic blocks of the P2-FO profile (Fig. 6b and Tab. 2). The corresponding
277 Ki ratios vary from 0.55 to 0.03 (Tab. 2). The amounts of Fe_2O_3 and TiO_2 are also relatively
278 enriched in the nodules of the blocky duricrust from the P2-FO profile, with maxima of 25.9
279 wt.% and 2.82 wt.%, respectively (Table 2). The IOL varies from 74.6% in the loose matrix to
280 97.8% in the bauxitic blocks (Tab. 2) indicating moderate to strong lateritization (Fig. 7). The
281 maximum IOL value implies a near-complete leaching of silica relative to Al_2O_3 and Fe_2O_3,
282 while the minimum IOL value correlates with higher silica content in the loose matrix (Fig. 7

283 and Tab. 2). The CIA and MIA values reaches maximum of 90.5% and 92.3%, respectively
284 (Fig. 6c and Tab. 2) confirming a near-complete leaching of alkali and alkaline earth elements
285 from plagioclases, and Mg from pyroxenes.

286 The amounts of Al_2O_3 and Fe_2O_3 of the massive bauxite duricrust (B12) reach up to
287 51.80 wt.% and 25.50 wt.%, respectively (Fig. 6b and Tab. 2). The corresponding
288 mineralogical composition (Tab. 1) indicates highest contents of gibbsite (66%), followed by
289 goethite (30%), and hematite (9%). The Ki factor decreases from the bottom to the surface of
290 the horizon and reaches the lowest value (0.01) of the weathering sequence (Tab. 2). The CIA
291 and MIA also show the highest values, 90.9% and 92.4%, respectively (Fig 6c and Tab. 2).
292 The IOL of 99.2% indicates complete silica leaching, depletion of labile elements and strong
293 lateritization (Fig. 6c and Fig. 7) including also illuviation of clay ferruginous fine matter
294 (Fig. 4e).

295 The surface nodular bauxitic horizon (B11) shows decreasing Al_2O_3 content from
296 46.30 wt.% in the fragmented duricrust to 26.70 wt.% in the loose matrix, and Fe_2O_3 content
297 from 21.90 wt.% to 17.55 wt.% relative to the underlying massive bauxite (P2-FO; Fig. 6b
298 and Tab. 2). An increasing trend is noticed for SiO_2 up to 19.25 wt.% in the loose matrix.
299 Consequently, IOL decreases to 69.7% with increasing SiO_2 and kaolinite (Figs. 6b and 6c;
300 Fig. 7) relative to the underlying massive duricrust (Tabs. 1 and 2). The resulting weakly
301 lateritized loose matrix may enrich in SiO_2 at the surface of profiles (ex: P2-FO) by quartz
302 allochthonous input. This results in a Ki factor up to 0.72 and slight decreases of CIA (82.6%)
303 and MIA (69.7%) at the surface of the weathering sequence (Tab. 2).

304 In the downslope profile (P4-FO), Al_2O_3 contents are similar as those of the plateau
305 profiles (Tab. 2), but SiO_2 contents are higher (up to 14.40 wt.% in the duricrusted matrix).
306 This corresponds to 28% of kaolinite (Tab. 1) and a Ki factor up to 0.37 (Tab. 2). The Fe_2O_3

content is lower than that of the plateau profiles (~17%) with low goethite amounts (7% to 16%; Tab. 1). The massive bauxitic pebbles clearly differ from the cementing duricrusted matrix with the highest Al_2O_3 content of the profile (53.50 wt.%) and lowest silica content (2.02 wt.%). The CIA and MIA values are similar to those of the plateau profiles while IOL is low in the porous bauxitic duricrust (79.8%) compared to the plateau profiles (Tab. 2). The surface horizon of this profile shows the same composition as that of the plateau profiles with possible allochthonous enrichment of quartz.

4.3. Trace elements distribution across the weathering profiles sequence

The concentrations of trace elements are presented in Table 3 and variations relative to the trachyte composition are shown in the figure 8. The vertical evolution of some elements (Fig. 6) is also shown in the upslope composite profile (P2-FO + saprolite of P3-FO). These data first evidence that Nb and Zr are the most abundant trace elements, followed by Ga, Cr and V. Two groups of elements are distinguished based on their relative behavior compared to parent rock composition and their distribution along the profiles of the weathering sequence.

The first group comprises Nb, Zr, Ga, Cu, Ni, Co, Cr, V, As, Pb, Th, Hf, U and Ta, which are all enriched relative to the trachyte composition (Fig. 8; Tab. 3). Among these elements, Nb, Zr, Ga, Th, Hf, Ta are highly correlated (Fig. 6d and Figs. 9a to 9f). Their highest contents are recorded in the saprolite, the massive and bauxitic pebbly duricrusts while the lowest contents are measured in the blocky and nodular bauxitic horizons (Figs. 6, 8 and Tab. 3). These compositions including high field strength elements (HFSE: Zr, Hf, Nb, Ga and Ta) suggest their relative stability during weathering and lateritization (Zarasvandi et al., 2012) as commonly observed in bauxites developed from lateritic weathering of alkaline parent rocks (Mordberg, 1996). Moreover, Nb, Zr, Ga, Th, Hf, U, and Ta are correlated to TiO_2 (Tab. 4 and Figs. 9e to 9g), suggesting anatase as potential mineral carrier. Significant

positive correlations are also noticed between U, Ta and P_2O_5 (Tab. 4; Fig. 9h) indicating possibly florencite as host mineral (Fig; 5). On the other hand, the poor correlation between Al_2O_3 and some relatively enriched trace elements (Nb, Zr, Ga, Hf, Th, Ta; Tab. 4) indicates little gibbsite control in their distribution. This is explained by the low capacity of Al isomorphic replacement by trace elements in the structure of gibbsite (Mordberg, 1986).

Cu, Sc and Ni also exhibit similar behaviors and highest contents in the saprolite, the blocky bauxitic duricrust and the nodular bauxitic horizon, while the lowest contents are measured in the massive bauxitic duricrust (P2-FO; Figs. 6e and 8, and Tab. 3). These elements originate from the alteration of plagioclases and pyroxenes (Boski and Herbosch, 1990). According to Sahoo et al. (1980) and Trescases (1973), their high enrichment in the lowermost horizons of the profiles owes to downward translocation followed by their trapping in neoformed minerals. The moderate positive Spearman correlation with SiO_2 (Tab. 4) indicates little affinity with kaolinite (Lopez et al., 2005).

Co, Cr, and V show their highest contents in the blocky bauxitic duricrust and the nodular bauxitic horizon, and their lowest contents in the saprolite and the massive bauxitic duricrust (P2-FO; Figs. 6e-f, and 8; Tab. 3). Their behavior is primarily linked to the weathering of plagioclases, pyroxenes and Ti-magnetite, and secondarily to potential trapping by iron oxides. For example, Co is possibly controlled by goethite as indicated by the Spearman correlation coefficient with Fe_2O_3 (see e.g., Beauvais and Roquin, 1996; Moshood et al., 2006).

The second group comprises Y, Sr, Rb, Ba, and Zn, which are all depleted relative to the trachyte (Fig. 8 and Tab. 3), showing a decreasing trend from the saprolite to the massive bauxitic ducricrust, and a slight increase toward the surface. Their highest content is noticed with important Zn at the bottom of the massive bauxitic duricrust (Figs. 6f and 8b, Tab. 3).

Their leaching along the sequence is due to the weathering of plagioclases (Babechuck et al, 2014; Calagari et al., 2010), as reflected by strong positive Spearman correlations between Rb and alkali and alkaline earth elements (Tab. 4). Sr, Ba and Zn are further enriched in the saprolite relative to the uppermost duricrusted horizons (Figs. 6f and 8c) due to downward leaching (Mordberg, 1996) and their partial retention in kaolinite-rich horizons as indicated by the positive Spearman correlation with SiO_2 (Tab. 4; Plank and Langmuir, 1988).

Finally, Rb, Cu, Ni, Co, V and As are significantly enriched in the surface horizons (B11) compared to the underlying bauxites (Figs. 8a to 8c), which potentially reflect importation of bearing heavy minerals. The overall distribution of trace elements depends on secondary mineral formation (mainly kaolinite, goethite and anatase) and thus upon the intensity of lateritization, with no geomorphic control along the sequence.

4.4. Rare earth elements fractionation across the weathering profiles sequence

REE abundance varies from 49 µg/g to 1790 µg/g (Tab. 5). Saprolite and massive bauxitic horizon exhibit maximum contents while minimum REE concentrations are mostly measured in the other horizons (e.g. upslope profile P2-FO; Fig. 6g). Light rare earth elements (LREE) are the most abundant (∑LREE from 47 µg/g to 1746 µg/g) compared to heavy rare earth elements (HREE) (∑HREE from 2 µg/g to 44 µg/g; Tab. 5). Their overall behavior along the sequence evidence maximum contents in the upslope profile (P2-FO; ∑REE up to 1102 µg/g) compared to other profiles (Tab. 5).

Spearman rank correlations calculated between REE and major elements reflect potential host minerals (Braun et al., 1993). The lack of correlation between REE and Al_2O_3 or TiO_2 (Tab. 4) indicates no influence of gibbsite and anatase. REE are negatively correlated with Fe_2O_3 and weakly correlated with SiO_2 (Tab. 4) suggesting little control from kaolinite (Babechuck et al., 2014; Zarasvandi et al., 2012). Positive correlations between REE and P_2O_5

(Tab. 4) suggest potential phosphates host minerals (Putzolu et al., 2018). Although concentration < 5% is a limit for XRD identification, XRD peaks ($d_{h,k,l}$ ~ 5.71 Å, 2.93 Å and 2.17 Å) suggest that florencite (Figs. 5b-c; see P2-FO-5 and P3-FO-3) is a potential carrier of LREE (La and Nd).

The C1 chondrite normalized REE (Mc Donough and Sun, 1995) for trachyte and weathered samples are similar and evidence REE enrichment relative to Chondrite across the profiles sequence. LREE are strongly enriched compared to HREE (Fig. 10). The normalized spectra further evidence REE depletion relative to trachyte along the sequence, except in the saprolite and the upslope profile P2-FO (Fig. 10).

Two anomalies, Eu and Ce, are highlighted. The positive Eu anomaly in the trachyte and the saprolite (Fig. 10c) is linked to plagioclases, which bear Eu (Babechuck et al., 2014). However, negative Eu anomaly is noticed across the sequence from the bottom to the top of duricrusted lateritic horizons (Fig. 10) implying a progressive Eu leaching during lateritization, as previously shown in weathering profiles derived from basalts (Babechuck et al., 2014). Although a negative Ce anomaly is clearly defined in saprolite (Fig 10c), a positive anomaly is rather noticed across the sequence, except in the upslope profile P2-FO (Fig. 10b).

Calculated Eu/Eu* and Ce/Ce* anomalies are in agreement with chondrite normalized patterns. Eu/Eu* values extend from a maximum of 1.28 in the trachyte, 1.09 in the saprolite, and 0.60 in duricrusted horizons of the plateau profiles (Tab. 5) due to the quick weathering of plagioclases; while the minimum value of 0.42 is noticed in bauxitic pebbles of the downslope profile (P4-FO; Tab. 5). Ce/Ce* values vary from 0.99 in the trachyte to a minimum of 0.53 in the saprolite (Tab. 5). Maximum values (up to 4.89) are further measured in the massive bauxitic duricrust indicating Ce enrichment relative to La and Pr. The

403 scatterplot between Ce/Ce* and ∑REE (Fig. 11a) also indicates Ce enrichment during
404 lateritization.

405 The La/Y ratio varies from 1.50 to 9.12 along the sequence (Tab. 5; Fig. 11b) that
406 characterizes REE fractionation during the weathering process. The highest values measured
407 in the saprolite, the massive and bauxitic pebbly duricrusts correlate with the highest REE
408 content, while the lowest values correlate with lowest REE content in the other horizons of
409 the profiles sequence (Tab. 5). This behavior may suggest REE depletion with pH decrease
410 (Maksimovic and Panto, 1991; Zarasvandi et al., 2012) inferring potential effect of pH
411 variations during bauxitic weathering. The $(La/Yb)_N$ ratio of saprolite is the highest (68.4),
412 and varies in the profiles from 40.8 in the massive bauxite to lower values (7.8) in the surface
413 nodular bauxitic and fine earthy horizon (Table 5). Despite the poor correlation between
414 $(La/Yb)_N$ and CIA, the broad correlation in the massive bauxite (Fig. 11c) suggests increasing
415 $(La/Yb)_N$ with the weathering intensity (Ndjigui et al., 2008). This trend is confirmed in
416 scatterplots $(La/Yb)_N$ vs. $(Gd/Yb)_N$ and (Eu/Eu*) vs. $(Gd/Yb)_N$ (Fig. 11d and 11e), which also
417 indicate REE fractionation with increasing lateritization. The overall REE composition is
418 strongly correlated to that of trace elements (Fig. 11f) that suggests common host minerals
419 and/or similar geochemical behaviors along the weathering sequence to some extent.
420

421 **4.5. Major pattern of bauxite formation and evolution**

422 Geochemical analyses and chondrite normalized REE spectra of weathering samples
423 document that lateritic weathering profiles formed by in-situ weathering of trachyte. Saprolite
424 formation consists in pseudomorphic weathering of parent rock minerals implying strong
425 leaching of labile elements and in-situ formation of kaolinite, while plagioclases and cpx
426 weathered into gibbsite and goethite, respectively. Low Ki value (0.77) indicates a kaolinite-
427 rich weathering, with noticeable amount of primary gibbsite both formed under humid

climatic conditions (Beauvais, 1999, 2009; Tardy and Roquin, 1998) and optimal drainage of the profiles sequence (Bocquier et al., 1983; Yongué-Fouateu, 1986). The interconnected porosity observed in saprolite results from eluviation processes of its clayey matrices (Nahon, 1991; Tardy and Nahon, 1985).

The structural, mineralogical and geochemical characteristics of the blocky bauxitc duricrust document the disaggregation process of the overlying massive duricrust, which is characterized by Fe-depletion from clayey matrices during seasonal changes of the water table level (Ambrosi and Nahon, 1986; Boulangé, 1984; Tardy, 1997; Tematio and Olson, 1997). This results in less cohesiveness and more fragmentation and disaggregation of massive duricrust (Beauvais and Tardy, 1993; Beauvais, 2009; Hieronymus et al., 1999; Soares de Oliveira et al., 2013). The Ki value of 0.03 in the bauxitic blocks highlights intense bauxitization implying near-complete silica leaching under hot and very wet climatic weathering conditions (Boulangé, 1984; Tardy and Roquin, 1998). However, highest value (0.54 in the loose matrix) indicates less leaching of the upper duricrusted horizons (Hieronymus, 1973; Soares de Oliveira et al., 2013).

The massive bauxitic duricrust has the lowest Ki ratio of the sequence (0.01) typifying very strong bauxitization process with complete silica depletion and increasing chemical weathering intensity (Hiéronymus, 1973; Nyobe, 1987; Tematio et al., 2009). Aluminum enrichment at this stage does not only result from relative accumulation after labile element depletion, but also from secondary illuviation process (Eschenbrenner, 1987; Mutakyahwa et al., 2003), which is illustrated by cutans and/or complete infilling of voids with secondary gibbsite crystallizations in the massive bauxite. The elongated dark brown domains at the bottom of this massive duricrusted horizon result from late pedogenetic process involving

water table level variations, which preferentially mobilizes and concentrates iron into goethite (Hieronymus, 1973; Beauvais, 1999).

The duricrust disaggregation mechanism in the surface nodular bauxitic horizon is similar to that of the blocky bauxite, implying Fe mobility (Beauvais, 2009), and potential downward Al enrichment and maturation of massive bauxite by secondary gibbsite crystallization. Silica enrichment on top of profile sequence may be assigned to possible aeolian inputs (Brimhall et al., 1991).

The loose and heterogeneous structures of the lateritic materials from the downslope profile with lower IOL values than in the plateau profiles typify a reworked allochthonous formation resulting from erosion and redistribution of various sized fragments of bauxites and/or Fe lateritic crusts on gently sloping surfaces (Beauvais et al., 2003; Boulangé, 1984; Chardon et al., 2018; Eno Belinga, 1972; Grimaud et al., 2015; Momo Nouazi et al., 2012). Such an erosion feature may have occurred after incision of the initial bauxitic surface, which was potentially favored by combined Pliocene surface uplift (Morin, 1985) and climate change from humid to drier conditions (Ruddiman et al., 1989) that triggered mechanical erosion of bauxite and redistribution of bauxitic elements in the landscape. Given that the Fongo-Tongo trachytes erupted during the Burdigalian ca. 16 Ma ago (Nkouathio et al., 2006), intense bauxitic weathering illustrated by primary gibbsite formed by weathering of plagioclase was first initiated in mid-Miocene under warm and humid climatic conditions correlated to high chemical marine sedimentation (Davies et al., 1977). Then, former bauxitic weathering profiles possibly maturated by massive secondary gibbsite formation/crystallization in discontinuities and porosities in Late Miocene before their dismantling by mechanical erosion from Pliocene, which was also a period of continental dust fluxes and high clastic sedimentation in offshore basins (Van Andel et al., 1977).

5. Conclusion

Neogene lateritic weathering of trachyte from the Bambouto volcanics led to the formation and differentiation of lateritic bauxitic profiles that preserved basically the trachytic structure from the saprolites to the top of profiles. Weathering of parent minerals results in strong leaching of labile elements, relative or absolute enrichment of alumina from 34.3 wt% up to 53.5 wt.% in the saprolite and duricrusted horizons, respectively, and consecutive formation of gibbsite and goethite with lesser kaolinite. During lateritic bauxitization, both mineralogical and geochemical differentiations control the trace elements behavior and REE fractionation across the weathering profiles, with major contents upslope in the sequence. Pliocene degradation of the bauxite and/or dissection or dismantling of bauxitic landscapes previously formed during mid- to upper Miocene resulted in Fe-depletion, and allochthonous silica enrichment on top of lateritic profiles. Accounting for major geochemical and morphological differentiation of the Fongo-Tongo bauxitic weathering landscapes usefully document the evolving dynamics of lateritic regolith and landsurfaces in Cameroon.

Acknowledgements

The financial support for mineralogical and geochemical data of this study was provided by the Service de Coopération et d'Action Culturelle de la France au Cameroun (SCAC) (815364G). The mineralogical analyses have been carried out at the Centre Européen de Recherche et d'Enseignement des Géosciences de l'Environnement (CEREGE), Aix Marseille University, OSU Pytheas, France; the geochemical analysis has been carried out at ALS Laboratory Group SL-Spain. AB and J-PA are supported by IRD and CNRS, respectively. Two anonymous reviewers are thanked for their comments that help improving the structure of the paper.

500 ## References

501 Ambrosi, J.P., Nahon, D., 1986. Petrological and geochemical differentiation of lateritic iron
502 crust profiles. Chemical Geology 57, 371-393.

503 American Mineralogist Crystal Structure Database, 2016.
504 http://rruff.geo.arizona.edu/AMS/amcsd. php (accessed 06.08.17).

505 Babechuk, M.G., Widdowson, M., Kamber, B.S., 2014. Quantifying chemical intensity and
506 trace element release from two contrasting profiles, Decan Traps, India. Chemical Geology
507 365, 56-75.

508 Ballentine, C.J., Lee, D.C., Halliday, A. N., 1997. Hafnium isotopic studies of the Cameroon
509 Line and new HIMU paradoxes. Chemical Geology 139, 111-124.

510 Beauvais, A., 1999. Geochemical balance of lateritization processes and climatic signaturs in
511 weathering profiles overlain by ferricretes in Central Africa. Geochimica et Cosmochimica
512 Acta, 63 (1999), pp. 3939-3957.

513 Beauvais, A., 2009. Ferricrete biochemical degradation on the rainforest savannas boundary
514 of Central African Republic. Geoderma 150, 379-388.

515 Beauvais, A., Chardon, D., 2013. Modes, tempo, and spatial variability of Cenozoic cratonic
516 denudation: The West African example. Geochemistry, Geophysics, Geosystems 14 (5),
517 1590-1608. doi:10.1002/ggge.20093.

518 Beauvais, A., Ritz, M., Parisot, J-C., Bantsimba, C., 2003. Testing etching hypothesis in
519 shaping granite dome structures beneath lateritic weathering landsurfaces using ERT
520 method. Earth Surface Processes and Landforms 28 (10), 1071-1080.

521 Beauvais, A., Roquin, C., 1996. Petrological differentiation patterns and geomorphic
522 distribution of ferricretes in Central Africa. Geoderma 73, 63-82.

523 Beauvais, A., Tardy, Y., 1993. Degradation and dismantling of iron crusts under climatic
524 changes in Central Africa. Chemical Geology 107, 277-280.

525 Bocquier, G., Boulangé, B., Ildefonse, P., Nahon, D., Muller, D., 1983. Transfers,
526 accumulation modes, mineralogical transformation and complexity of historical
527 development in lateritic profiles. International Symposium on Laterisation. Proceeding.,
528 Sao Paulo., AJ. Melii et A. Carvahlo éds. 2, 331-343.
529 Boulangé, B., 1984. Les formations bauxitiques latéritiques de Côte d'Ivoire. Les faciès, leur
530 transformation, leur distribution et l'évolution du modelé. Thèse et Mémoire ORSTOM
531 363 pp.
532 Boulangé, B., Ambrosi, J.-P. and Nahon, D., 1997. Laterites and Bauxites. In: H. Paquet and
533 N. Clauer (Editors), Soils and Sediments: mineralogy and geochemistry. Springer Berlin
534 Heidelberg, pp. 49-65.
535 Boski, T., Herbosch, A., 1990. Trace elements and their relation to the mineral phases in
536 lateritic bauxites from Se Guinea Bissau. Chemical Geology 82, 279-297.
537 Braun, J.-J., Pagel, M., Herbillon, A., Rosin, C., 1993. Mobilization and redistribution of
538 REEs and thorium in a syenitic lateritic profile: a mass balance study. Geochimica et
539 Cosmochimica Acta 57, 4419-4434.
540 Brewer, R., Sleeman, J. R., 1988. Soil Structure and Fabric. CSIRO Australia, Melbourne,
541 173 pp.
542 Brimhall, G.H., Lewis, C.J., Ford, C., Bratt, J., Taylor, G., Warin, O., 1991. Quantitative
543 geochemical approach to pedogenesis: importance of parent material reduction, volumetric
544 expansion, and eolian influx in lateritization. Geoderma 51, 51-91.
545 Calagari, A.A., Kangarini Farahani, F., Abedini, A., 2010. Geochemistry on major, trace and
546 rare earth elements in Biglar Permo-Triasic bauxite deposit, Northwest of Abgarm,
547 Ghazvin Province, Iran. Journal of Sciences, Islamic republic of Iran 21 (3), 225-236.

548 Cameroon Alumina LTD., 2008. Etude d'Impact Environnemental et Social du projet
549 d'exploitation des gisements de bauxite de Minim-Martap et Ngaoundal dans la Région de
550 l'Adamaoua, République du Cameroun. Résumé exécutif. pp 39.
551 Chardon, D., Grimaud, J.L., Beauvais, A., Bamba, O., 2018. West African lateritic pediments:
552 Landform-regolith evolution processes and mineral exploration pitfalls. Earth science
553 reviews 179, 124-146.
554 Colin, F., Beauvais, A., Ambrosi, J-P., Nahon, D., 2004. Les latérites en environnement
555 tropical, source de métaux d'intérêt économique. Assises de la Recherche Française dans le
556 Pacifique, Nouméa, pp. 104-107.
557 Davies, T.A., Hay, W.W., Southam, J.R., Worsley, T.R., 1977. Estimates of cenozoic oceanic
558 sedimentation rates. Science 197, 53-55.
559 Déruelle, B., Moreau, C., Nkoumbou, C., Kambou, R., Lissom, J., Njonfang, E., Ghogomu,
560 R.T., Nono, A., 1991. The Cameroon Line: a review. In: Kampunzu AB, Lubala RT (eds)
561 Magmatism in extensional structural settings. Springer, Berlin, pp. 274-327.
562 Duzgoren-Aydin, N.S., Aydin, A., Malpas, J., 2002. Re-assesment of chemical weathering
563 indices: case study on pyroclastic rocks of Hong-Kong. Engineering geology 63, 99-119.
564 Eno Belinga, S.M., 1972. L'altération des roches basaltiques et le processus de bauxitisation
565 dans l'Adamaoua (Cameroun). Thèse de Doctorat, Université de Paris, pp 571.
566 Eschenbrenner, V., 1987. Les glébules des sols de Côte d'Ivoire. Thèse ès Sciences,
567 Université de Bourgogne, Dijon, 2 t,. pp 496.
568 Grandin, G., 1976. Aplanissements cuirassés et enrichissement des gisements de manganèse
569 dans quelques régions d'Afrique de l'Ouest. Mémoire de l'ORSTOM 82, 1-275.
570 Grimaud, J-L., Chardon, D., Metelka, V., Beauvais, A., Bamba, O., 2015. Neogene cratonic
571 erosion fluxes and landform evolution processes from regional regolith mapping (Burkina
572 Faso, West Africa). Geomorphology 241, 315-330. Doi :10.1016/j.geomorph.2015.04.006.

573 Hiéronymus, B., 1973. Etude minéralogique et géochimique des formations bauxitiques de
574 l'Ouest Cameroun. Cahier de l'ORSTOM, Série Géologie 1, 97-112.
575 Hieronymus, B., Kotschoubey, B., Godot, J.-M., Boulègue, J., 1999. Evolução atual da
576 cobertura laterítico-bauxítica da serra de Trucará, baixo rio Tocantins, Pará. Revista
577 Brasileira de Geociencias 29 (4), 649-656.
578 Irfan, T.Y., 1999. Characterisation of weathered volcanic rocks in Hong Kong. Quarterly
579 Journal of Engineering Geology and Hydrogeology 32, 317-348.
580 Kagou Dongmo, A., Nkouathio, D.G., Pouclet, A., Bardintzeff, J-M., Wandji, P., Nono, A.,
581 Guillou, H., 2010. The discovery of Late Quaternary basalt on Mount Bambouto:
582 implications for recent widespread volcanic activity in the southern Cameroon Line.
583 Journal of African Earth Sciences 57, 96-108.
584 Kengni, L., Tekoudjou, H., Tematio, P., Tedonkeng, E.P., Mubeteneh Tankou, C., 2009.
585 Rainfall Variability along the Southern Flank of the Bambouto Mountain (West-
586 Cameroon). Journal of the Cameroon academy of sciences 8, 45-52.
587 Kwékam, M., Liégeois, J.P., Njonfang, E., Affaton, P., Hartmann, G., 2010. Nature, origin
588 and significance of the Fomopéa Pan-African high-K calc-alkaline plutonic complex in the
589 Central African fold belt (Cameroon). Journal of African Earth Sciences 57, 79-95.
590 Lopez J.M.G., Bauluz, B., Fernandez-Nieto, C., Oliete, A., 2005. Factors controlling the trace
591 element distribution in fine-grained rocks: the Albian kaolinite-rich deposits of the Oliete
592 Basin (NE Spain). Chemical Geology 214, 1-19.
593 Mc Donough, W.F., Sun, S.S., 1995. The composition of the Earth. Chemical Geology 120,
594 223-253
595 Maksimovic, Z., Panto, G., 1991. Contribution to the geochemistry of the rare earth elements
596 in the karst-bauxite deposits of Yugoslavia and Greece. Geoderma 51, 93-109.

597 Momo Nouazi, M., 2016. The lateritic surfaces on the Bamiléké Plateau (West Cameroon):
598 bauxitic potential mapping, genetic processes, morphotectonic analysis and implication on
599 landscape dynamics. Ph.D Thesis, University of Dschang, pp 223.
600 Momo Nouazi, M., Yemefack, M., Tematio, P., Beauvais, A., Ambrosi, J-P., 2016.
601 Distribution of duricrusted bauxites and laterites on the Bamiléké plateau (West
602 Cameroon): Constraints from GIS mapping and geochemistry. Catena 140, 15-23.
603 Momo Nouazi, M., Tematio, P., Yemefack, M., 2012. Multiscale organization of the
604 Doumbouo-Fokoué Bauxites Ore Deposits (West Cameroun): Implication to the
605 Landscape Lowering. Open Journal of Geology 2, 14-24.
606 Mordberg, L.E., 1996. Geochemistry of trace elements in Paleozoic bauxite profiles in
607 northern Russia. Journal of Geochemical Exploration 57, 187-199.
608 Morin, S., 1985. Cuirasses et reliefs de l'ouest Cameroun. Laboratoire de géomorphologie du
609 CEGET/CNRS, 33405 Talence France. 11 p.
610 Moshood, N.T., Okunlola, O.A., Abimbola, A.F., 2006. Lithogenic concentrations of trace
611 metals in soils and saprolites over crystalline basement rocks: A case study from SW
612 Nigeria. Journal of African Earth Sciences 46, 427-438.
613 Mutakyahwa, M.K.D., Ikingura, J.R., Mruma, A.H., 2003. Geology and geochemistry of
614 bauxite deposits in Lushoto District, Usambara Mountains, Tanzania. Journal of African
615 Earth Sciences 36, 357-369.
616 Nahon, D., 1991. Introduction to the petrology of soils and chemical weathering. A Wiley-
617 Inter-science Publication, pp 313.
618 Nahon, D., 1986. Evolution of iron crusts in tropical landscapes. In: Rates of chemical
619 weathering of rocks and materials, S.M. Coleman and D.P. Dethier eds., Academic Press
620 Inc., pp. 169-191.

621 Ndjigui, P.D., Bilong, P., Bitom, D., Dia, A., 2008. Mobilization and redistribution of major
622 and trace elements in two weathering profiles developed on serpentinites in the Lomié
623 ultramafic complex, South-East Cameroon. Journal of African Earth Sciences 50, 305-328.
624 Nesbitt, H.W., Young, G.M., 1982. Early Proterozoic climates and plate motions inferred
625 from major element chemistry of lutites. Nature 279, 715-717.
626 Ngako, V., Njonfang, E., Tongwa Aka, F., Affaton, P., Metuk Nnange, J., 2006. The North-
627 South Paleozoic to Quaternary trend of alkaline magmatism from Niger-Nigeria to
628 Cameroon: Complex interaction between hotspots and Precambrian faults. Journal of
629 African Earth Sciences 45 (3), 241-256.
630 Nkouathio, D.G., Kagou Dongmo, A., Wandji, P., Bardintzeff, J.M., Tchoua, F.M., 2006.
631 Evolution and tectonic control of volcanism along the Cameroon Volcanic Line: case study
632 of graben and horst volcanoes. Implication on the nature of volcanic hazards. Garavolcan,
633 300th ?? International Conference commemorating the 1706 Arenas Negras Eruption,
634 Garachico, Tenerife, Canary Islands, May 22-27.
635 Nkouathio, D.G., Kagou Dongmo, A., Bardintzeff, J. M., Wandji, P., Bellon, H., Pouclet, A.,
636 2008. Evolution of volcanism in graben and horst structures along the Cenozoic Cameroon
637 Line (Africa): implications for tectonic evolution and mantle source composition.
638 Mineralogy and Petrology 94, 287-303.
639 Nono, A., Njonfang, E., Kagou Dongmo, A., Nkouathio, D. G., Tchoua F. M., 2004.
640 Pyroclastic deposits of the Bambouto volcano (Cameroon Line, Central Africa): evidence
641 of a strombolian initial phase. Journal of African Earth Sciences 39, 409-414.
642 Nyobe, J.B., 1987. A geological and geochemical study of the Fongo-Tongo and areally
643 related bauxites deposits, Western Highlands, Republic of Cameroun. PhD thesis, pp 352.
644 Plank, T., Langmuir, C.H., 1988. The chemical composition of subducting sediment and its
645 consequences for the crust and mantle. Chemical Geology 145, 325-394.

Putzolu, F., Papa, A.P., Mondillo, N., Boni, M., Balassone, G., Mormone, A., 2018. Geochemcial characterization of bauxite deposits from the Abruzzi mining district (Italy). Minerals 8, 298, doi:10.3390/min8070298.

Rietveld, H.M., 1969. A profile refinement method for nuclear and magnetic structures. Journal of Applied Crystallography 2, 65-71.

Ruddiman, W.F., Sarnthein, M., Backman, J., Baldauf, J.G., Curry,W., Dupont, L.M., Janecek, T., Pokras, E.M., Raymo, M.E., Stabell, B., Stein, R., Tiedemann, R., 1989. Late Miocene to Pleistocene evolution of climate in Africa and the low-Iatitude Atlantic: overview of Leg 108 results. Proceedings of the Ocean Drilling Program, Scientific Results, 108, (7), pp. 463-486.

Sahoo, R.K., Kaden, G.V.D., Muller, G., 1980. The mineralogy and geochemistry of nickeliferous laterite of Sukinda, Orissa, India. Proceeding of the 1st International Symposium on Laterites, Trivandrum, pp. 77-85.

Schellmann, W. 1994. Geochemical differentiation in laterite and bauxite formation. Catena 21, 131-143.

Soares de Oliveira, F., Chicarino Varajão, A.F.D., Chicarino Varajão, C.A., Boulangé, B., Vieira Soares, C.C., 2013. Mineralogical, micromorphological and geochemical evolution of the facies from the bauxite deposit of Barro Alto, Central Brazil. Catena 105, 29-39.

Tardy, Y., 1997. Petrology of Laterites and Tropical Soils. Balkema, Rotterdam, pp 408.

Tardy, Y., Nahon, D., 1985. Geochemistry of laterites, stability of Al-goethite, Al-hematite, and Fe^{3+}-kaolinite in bauxites and ferricretes : an approach to the mechanism of concretion formation. American Journal of Science 285, 865-903.

Tardy, Y., Roquin, C., 1998. Dérive des continents, Paléoclimats et altérations tropicales. B.R.G.M., pp 473.

Taylor, G., Eggleton, R.A., 2001. Regolith geology and geomorphology. Wiley, Chichester.

671 Taylor, R.G., Howard, K.W.F., 1998. Post-Paleozoic evolution of weathered landsurfaces in
672 Uganda by tectonically controlled deep weathering and striping. Geomorphology 25, 173-
673 192.
674 Tematio, P., Olson, K.R., 1997. Characterization of two phases of encrustment in a sequence
675 of ferrallitic soils in the South Cameroon and its effects on landscape evolution. Soil
676 Science, USA., 162 (10) 758-766.
677 Tematio, P., Fritsch, E., Hodson, M. E., Lucas, Y., Bitom, D., Bilong, P., 2009. Mineral and
678 geochemical characterization of a leptic aluandic soil and a thapto aluandic-ferralsol
679 developed on trachytes in Mount Bambouto (Cameroon volcanic line). Geoderma 152,
680 314-323.
681 Tematio, P., Meli, S., Leumbe Leumbe, O., Momo Nouazi, M., Yemefack, M., Yongue
682 Fouateu, R., 2015. Mapping bauxite indices using Landsat ETM+ imageries constrained
683 with environmental factors in Foumban area (West Cameroon). Journal of African Earth
684 Sciences 109, 47-54.
685 Traoré, D., Beauvais, A., Chabaux, F., Peiffert, C., Parisot, J.C., Ambrosi, J.P., Colin,
686 F., 2008a. Chemical and physical transfers in an ultramafic rock weathering profile: part 1.
687 Supergene dissolution of Pt-bearing chromite. American Mineralogist 93 (1), 22-30.
688 Traoré, D., Beauvais, A., Augé, T., Parisot, J.C., Colin, F., Cathelineau, M., 2008b. Chemical
689 and physical transfers in an ultramafic rock weathering profile: part 2. Dissolution vs.
690 accumulation of platinum-group minerals. American Mineralogist 93 (1), 31-38.
691 Trescases, J.J., 1973. L'évolution géochimique supergène des roches ultrabasiques en zone
692 tropicale - Formation des gisements nickélifères de Nouvelle Calédonie. Mémoire de
693 l'ORSTOM (Office de la recherche scientifique et technique outre-mer), Paris. 78, pp 259.

694 Ufer K., Stanjek H., Roth G., Dohrmann R., Kleeberg R., Kaufhold S., 2008. Quantitive
695 phase analysis of bentonites by the Rietveld method. Clays and Clay Minerals 56 (2), 272-
696 282.
697 Van Andel, T.H., Thiede, J., Sckater, J.G., Hay, W.W., 1977. Depositional history of the
698 South-Atlantic Ocean during the last 125 million years. J. Geol. 85 (6), 651-678.
699 Yongue-Fouateu, R., 1986. Contribution à l'étude pétrologique de l'altération et des faciès de
700 cuirassement ferrugineux des gneiss migmatitiques de la région de Yaoundé. Thèse
701 Doctorat 3ème cycle, Université de Yaoundé, 214 pp.
702 Zarasvandi, A., Carranza, E.J.M., Ellahi, S.S., 2012. Geological, geochemical and
703 mineralogical characteristics of the Deh-Now bauxite deposits, Zagros fold belt, Iran. Ore
704 geology reviews 48, 125-138.
705

706 **FIGURES CAPTION**

707 **Fig. 1**. **a)** Location and structure of the Cameroon Volcanic Line (from Ballentine et al., 1997;
708 and Ngako et al., 2006). **b)** Morphology and distribution of lateritic landsurfaces on the
709 Bamiléké plateau; **c)** Geological map of the Bamiléké plateau, Adapted from Kagou Dongmo
710 et al. (2010**)** and Nkouathio et al. (2008) (framed in Fig. 1b); **d)** Optical microscope
711 photomicrographs (crossed polarised light) of the porphyric trachyte highlighting a microlitic
712 assemblage of plagioclases (Pl), titanomagnetite (Tit) and large clinopyroxene (Cpx)
713 phenocrysts; **e)** Microlitic assemblage of Pl, Tit, and large phenocrysts of Cpx.

714

715 **Fig. 2**. Petrographical structure of the lateritic sequence **(a)**, and the weathering profiles **(b)**
716 highlighting the key features of structural changes.

717 **Fig. 3**. Petrographical structure of a field section and duricrusted samples. **a)** Vertical and
718 lateral view of upper profile. The dashed line is a limit between the bauxitic pebble horizon
719 (B11) at the top, and the massive bauxite duricrust (B12); **b)** Saprolitic duricrust and dark
720 brown domains (B12); **c)** and **d)** Massive bauxite duricrust (B12); **e)** Porous bauxite duricrust
721 (B15). **1**= saprolitic matrix, **2**= dark brown domain, **3**= reddish to yellow brown matrix, **4**=
722 void coated with yellowish cutans, **5**= reddish matrix, **6**= reddish crumbly infill, **7**= fine earth
723 infill.

724 **Fig. 4**. Micromorphology of the weathering structures. **a)** Saprolite; **b)** Blocky bauxite
725 duricrust; **c) and d)** Saprolitic duricrust with dark brown domains; **e)** and **f)** Massive bauxite
726 duricrust. 1= grey brown crystic fabric with primary gibbsite crystallization; 2= voids; 3=grey
727 argilic plasma; 4=reddish brown plasma; 5=grey crystic fabric with secondary gibbsite
728 crystallization; 6=grey argilic plasma; 7=dark brown argillic plasma; 8= Clay Fe-rich cutans.

729 **Fig. 5**. Mineralogical compositions from X-ray diffraction analyses. **a)** Plateau profile, **b)**
730 Upslope profile, **c)** Hillside profile, **d)** Downslope profile. San= sanidine; Aug= augite; an=
731 anorthite, Mi= microcline; Tit= Titanomagnetitte.

732 **Fig. 6.** Mineralogical and geochemical variations along the composite upslope profile (P2-FO
733 + saprolite). **a)** Mineralogical profile**; b)** Major oxides; **c)** Geochemical indices; **d), e)** and **f)**
734 Trace elements; **g)** Rare Earth elements. See figure 2 for the explanation of horizons in the
735 composite profile.

736 **Fig. 7.** SiO_2-Al_2O_3-Fe_2O_3 ternary plot illustrating the different degrees of lateritization in the
737 weathering sequence (after Schellman, 1994).

738 **Fig. 8.** Trachyte normalized trace elements spider diagrams of the weathering samples.

739 **Fig. 9**. Trace elements geochemical scattergrams. **a)** Th vs. Hf; **b)** Ta vs. Nb; **c)** Ta vs. Zr; **d)**
740 Ga vs. Hf; **e)** TiO2 vs. Zr; **f)** TiO2 vs. Hf; **g)** TiO2 vs. ∑Trace elements; **h)** P_2O_5 vs. U.

741 **Fig. 10.** Chondrite normalized REE spider diagrams of the weathering samples and the
742 trachyte

743 **Fig. 11.** REE geochemical scattergrams. **a)** ∑REE vs. Ce/Ce*; **b)** ∑REE vs. La/Y; **c)**
744 $(La/Yb)_N$ vs. CIA; **d)** $(La/Yb)_N$ vs. $(Gd/Yb)_N$; **e)** Eu/Eu* vs. $(Gd/Yb)_N$; **f)** ∑Trace elements vs.
745 ∑REE.

746

TABLES CAPTION

Table 1. Mineralogical composition obtained by quantitative Rietveld Refinement on the weathering facies. (-)=mineral present but below calculation limits, i.e. <5%; Ka=kaolinite; Bo=boehmite; Gi=gibbsite; Go=goethite; An=anatase; He=hematite; Ma=maghemite; Fl=Florencite; Qz=quartz. See Fig. 2 for description of horizons labels (B).

Table 2. Major elements (wt.%) and major elements mass change (%) in the weathering sequence. LOI=Loss Of Ignition; CIA (%)=Chemical Index of Alteration; IOL (%)=Index of Lateritization; MIA (%)=Mafic Index of Lateritization; Ki= Silica to aluminium ratio ($SiO_2/Al2O_3$); d.l.=Detection limits; (-)=Elements below detection limits. See Fig. 2 for description of horizons labels (B).

Table 3. Trace elements content (µg/g) of the weathering facies and the fresh rock. d.l.=Detection limits; (-)=Elements below detection limits. See Fig. 2 for description of horizons labels (B).

Table 4. Spearman's correlation coefficients of major elements with trace elements and REE (n=33).

Table 5. Rare earth elements content (µg/g) of the weathering facies and the fresh rock. d.l.=Detection limits. See Fig. 2 for description of horizons labels (B).

$Ce/Ce^* = (Ce_{sample}/Ce_{chondrite})/(La_{sample}/La_{chondrite})^{1/2} (Pr_{sample}/Pr_{chondrite})^{1/2}$

$Eu/Eu^* = (Eu_{sample}/Eu_{chondrite})/(Sm_{sample}/Sm_{chondrite})^{1/2} (Gd_{sample}/Gd_{chondrite})^{1/2}$

$(La/Yb)_N = (La_{sample}/La_{chondrite})/(Yb_{sample}/Yb_{chondrite})$

$(Gd/Yb)_N = (Gd_{sample}/Gd_{chondrite})/(Yb_{sample}/Yb_{chondrite})$

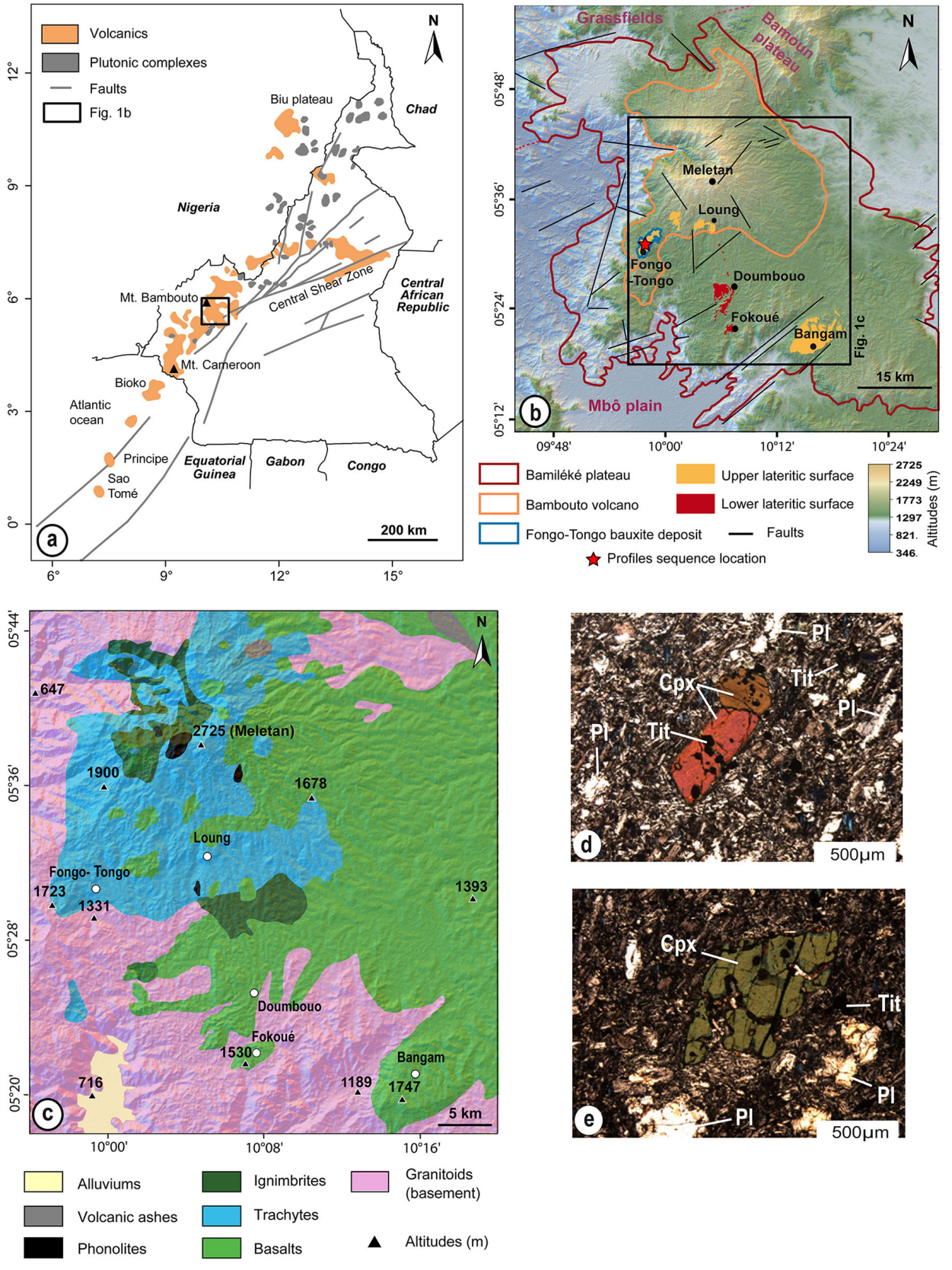
Volcanics
Plutonic complexes
Faults
Fig. 1b
Biu plateau
Chad
Nigeria
Mt. Bambouto
Central Shear Zone
Central African Republic
Mt. Cameroon
Bioko
Atlantic ocean
Principe
Sao Tomé
Equatorial Guinea
Gabon
Congo
200 km
a
Grassfields
Bamoun plateau
Meletan
Loung
Fongo -Tongo
Doumbouo
Fokoué
Bangam
Fig. 1c
15 km
Mbô plain
b
Bamiléké plateau
Bambouto volcano
Fongo-Tongo bauxite deposit
Profiles sequence location
Upper lateritic surface
Lower lateritic surface
Faults
Altitudes (m)
2725
2249
1773
1297
821.
346.
647
2725 (Meletan)
1900
1678
Loung
Fongo- Tongo
1723
1331
1393
Doumbouo
Fokoué
1530
Bangam
716
1189
1747
5 km
c
Alluviums
Volcanic ashes
Phonolites
Ignimbrites
Trachytes
Basalts
Granitoids (basement)
Altitudes (m)
Pl
Cpx
Tit
500µm
d
e

FIG. 1

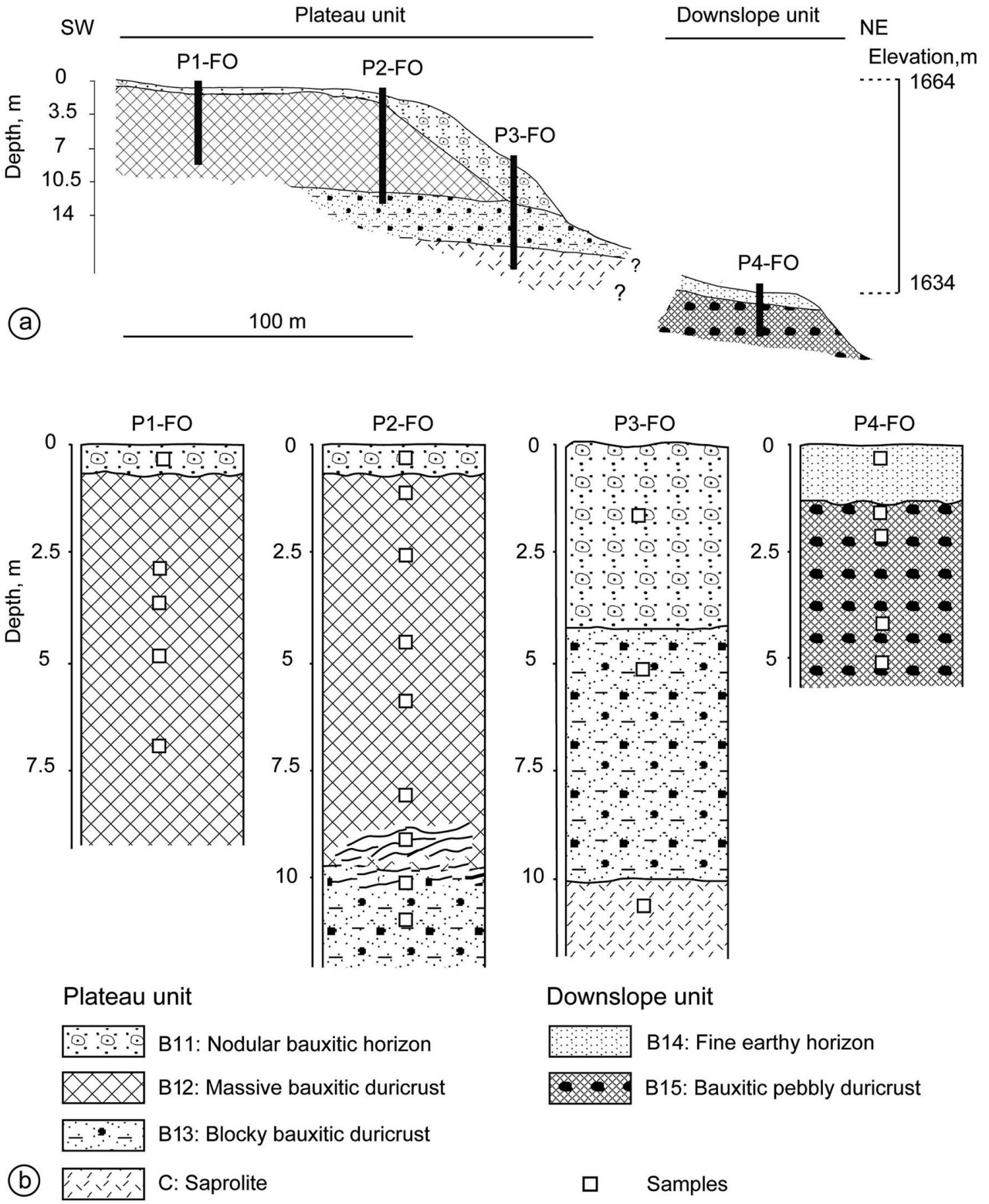
SW
Plateau unit
Downslope unit
NE
Elevation,m
1664
1634
P1-FO
P2-FO
P3-FO
P4-FO
Depth, m
0
3.5
7
10.5
14
?
?
a
100 m
P1-FO
P2-FO
P3-FO
P4-FO
Depth, m
0
2.5
5
7.5
10
Plateau unit
B11: Nodular bauxitic horizon
B12: Massive bauxitic duricrust
B13: Blocky bauxitic duricrust
C: Saprolite
Downslope unit
B14: Fine earthy horizon
B15: Bauxitic pebbly duricrust
Samples
b

FIG 2

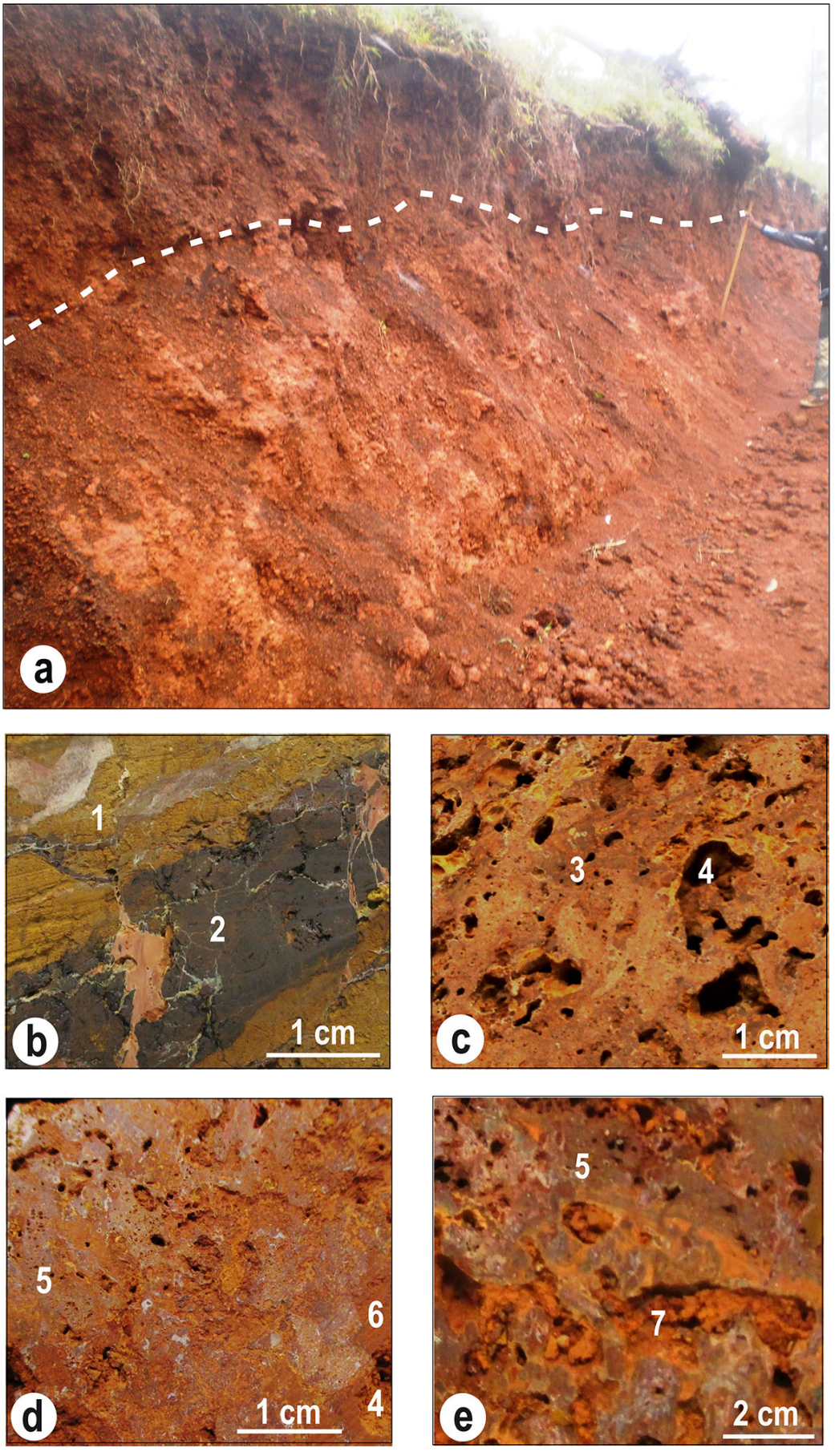

Fig. 3

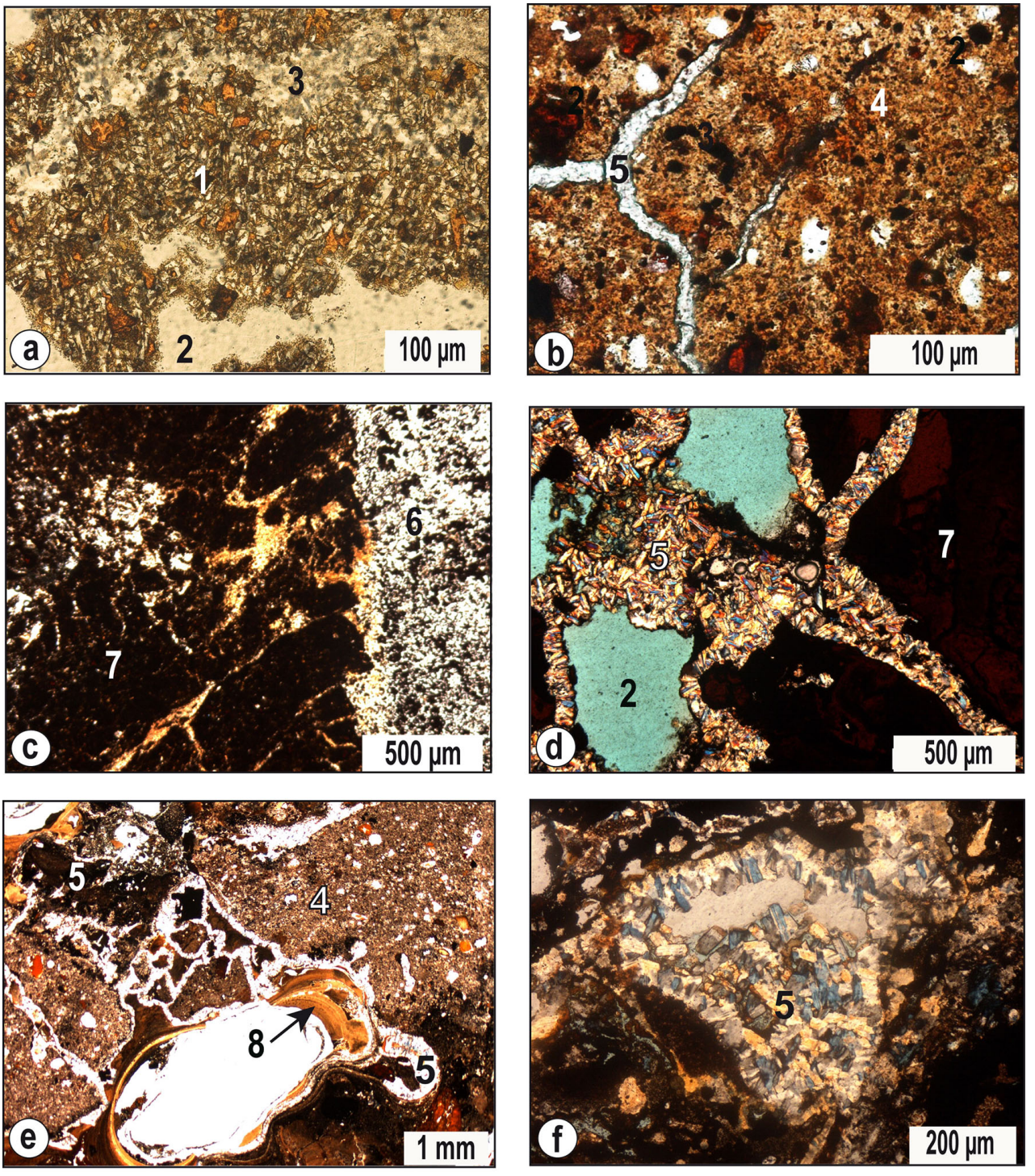
a
1
2
3
100 µm
b
2
2
3
4
5
100 µm
c
6
7
500 µm
d
2
5
7
500 µm
e
4
5
5
8
1 mm
f
5
200 µm

Fig. 4

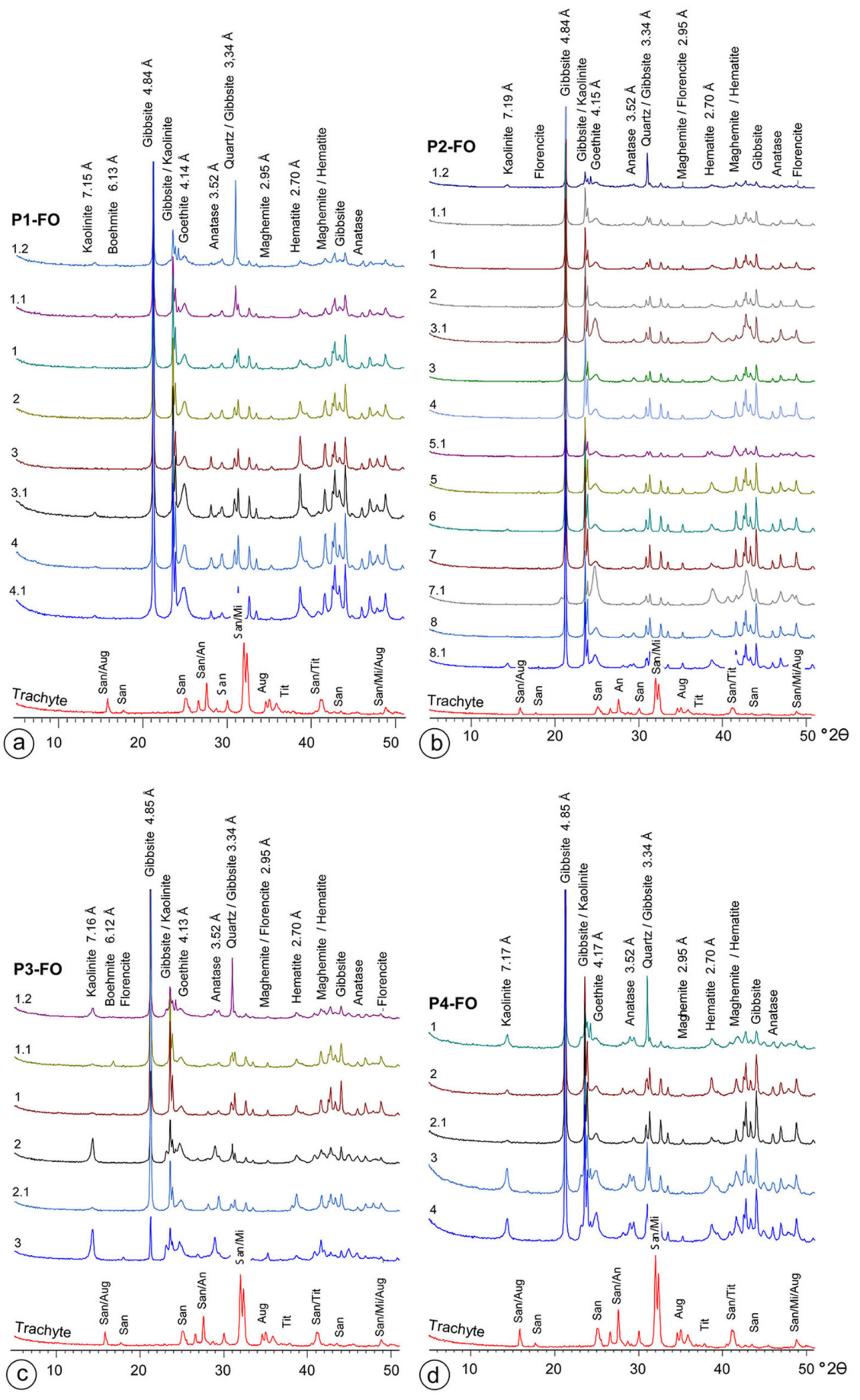
P1-FO
Kaolinite 7.15 Å
Boehmite 6.13 Å
Gibbsite 4.84 Å
Gibbsite / Kaolinite
Goethite 4.14 Å
Anatase 3.52 Å
Quartz / Gibbsite 3,34 Å
Maghemite 2.95 Å
Hematite 2.70 Å
Maghemite / Hematite
Gibbsite
Anatase
1.2
1.1
1
2
3
3.1
4
4.1
Trachyte
San/Aug
San
San
San/An
San
San/Mi
Aug
Tit
San/Tit
San
San/Mi/Aug
a
10
20
30
40
50
P2-FO
Kaolinite 7.19 Å
Florencite
Gibbsite 4.84 Å
Gibbsite / Kaolinite
Goethite 4.15 Å
Anatase 3.52 Å
Quartz / Gibbsite 3.34 Å
Maghemite / Florencite 2.95 Å
Hematite 2.70 Å
Maghemite / Hematite
Gibbsite
Anatase
Florencite
1.2
1.1
1
2
3.1
3
4
5.1
5
6
7
7.1
8
8.1
Trachyte
San/Aug
San
San
An
San
San/Mi
Aug
Tit
San/Tit
San
San/Mi/Aug
b
10
20
30
40
50
°2Θ
P3-FO
Kaolinite 7.16 Å
Boehmite 6.12 Å
Florencite
Gibbsite 4.85 Å
Gibbsite / Kaolinite
Goethite 4.13 Å
Anatase 3.52 Å
Quartz / Gibbsite 3.34 Å
Maghemite / Florencite 2.95 Å
Hematite 2.70 Å
Maghemite / Hematite
Gibbsite
Anatase
Florencite
1.2
1.1
1
2
2.1
3
Trachyte
San/Aug
San
San
San/An
San/Mi
Aug
Tit
San/Tit
San
San/Mi/Aug
c
10
20
30
40
50
P4-FO
Kaolinite 7.17 Å
Gibbsite 4. 85 Å
Gibbsite / Kaolinite
Goethite 4.17 Å
Anatase 3.52 Å
Quartz / Gibbsite 3.34 Å
Maghemite 2.95 Å
Hematite 2.70 Å
Maghemite / Hematite
Gibbsite
Anatase
1
2
2.1
3
4
Trachyte
San/Aug
San
San
San/An
San/Mi
Aug
Tit
San/Tit
San
San/Mi/Aug
d
10
20
30
40
50
°2Θ

FIG. 5

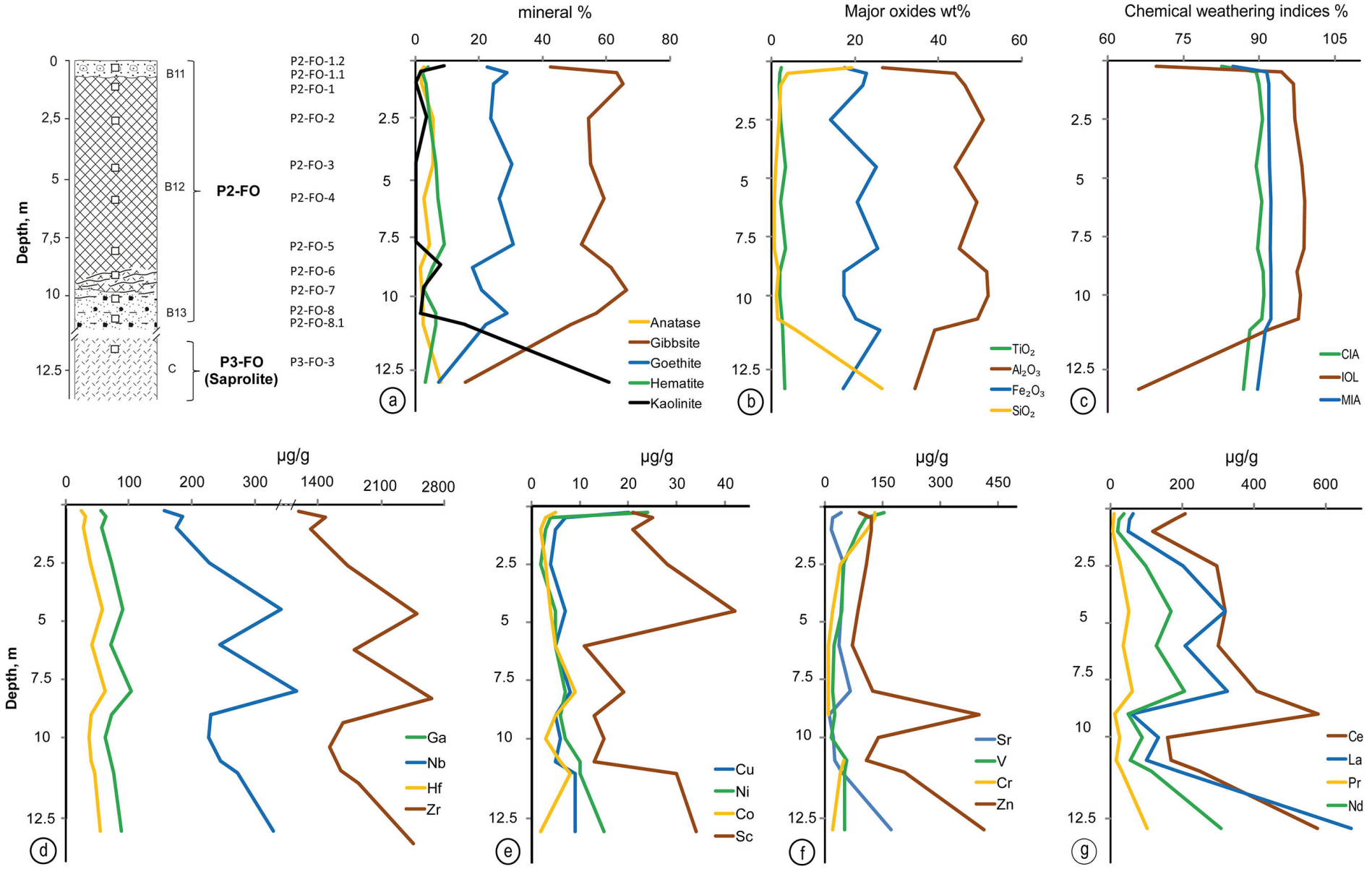
Depth, m
0
2,5
5
7,5
10
12.5
B11
B12
B13
C
P2-FO
P3-FO
(Saprolite)
P2-FO-1.2
P2-FO-1.1
P2-FO-1
P2-FO-2
P2-FO-3
P2-FO-4
P2-FO-5
P2-FO-6
P2-FO-7
P2-FO-8
P2-FO-8.1
P3-FO-3
mineral %
0 20 40 60 80
Anatase
Gibbsite
Goethite
Hematite
Kaolinite
a
Major oxides wt%
0 20 40 60
TiO2
Al2O3
Fe2O3
SiO2
b
Chemical weathering indices %
60 75 90 105
CIA
IOL
MIA
c
µg/g
0 100 200 300 1400 2100 2800
Ga
Nb
Hf
Zr
d
µg/g
0 10 20 30 40
Cu
Ni
Co
Sc
e
µg/g
0 150 300 450
Sr
V
Cr
Zn
f
µg/g
0 200 400 600
Ce
La
Pr
Nd
g

Fig 6

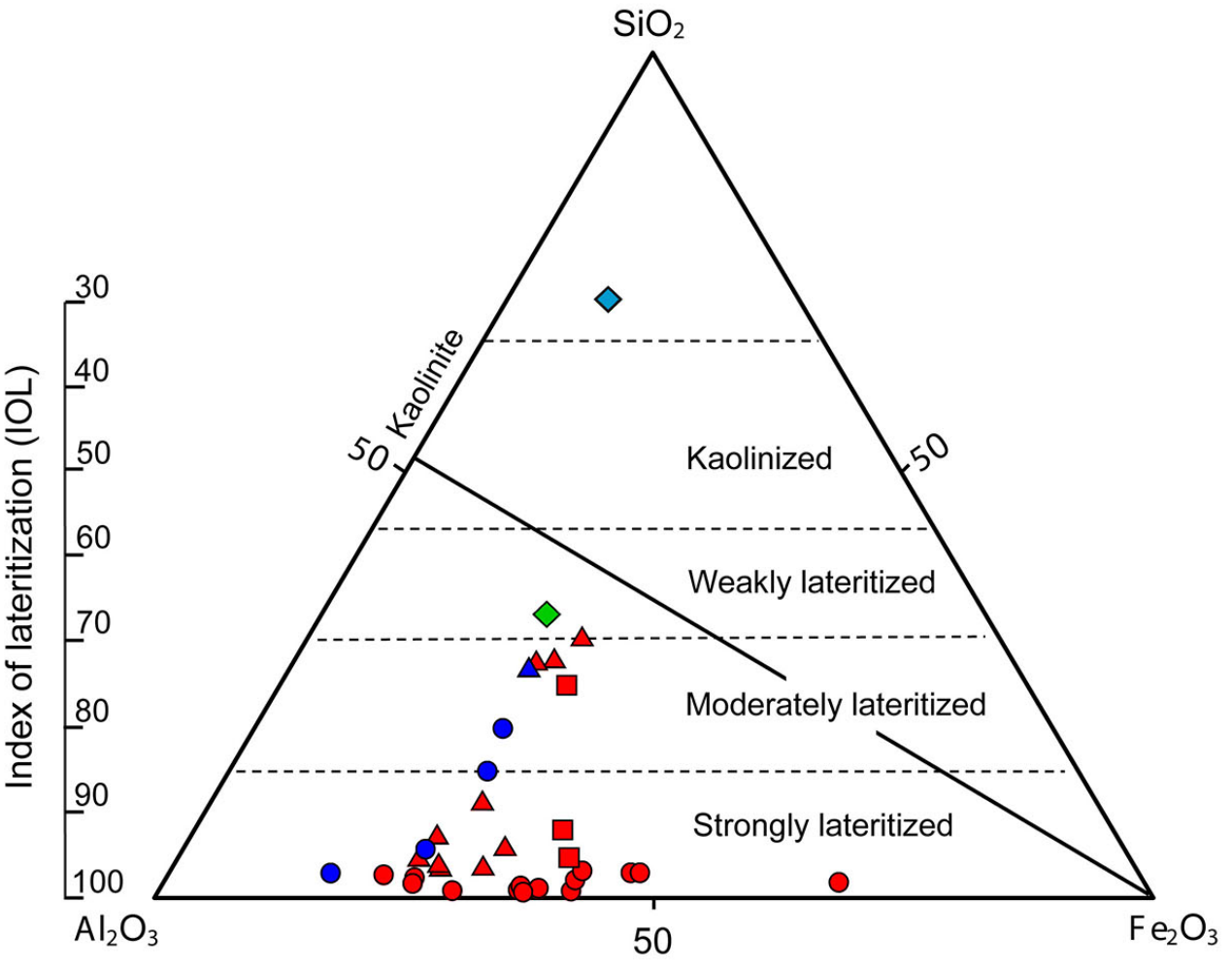

Plateau unit

- Nodular bauxitic horizon (B11)
- Massive bauxitic duricrust (B12)
- Blocky bauxitic duricrust (B13)

Downslope unit

- Fine earthy horizon (B14)
- Bauxitic pebbly duricrust (B15)

- Saprolite (C)
- Trachyte

FIG. 7

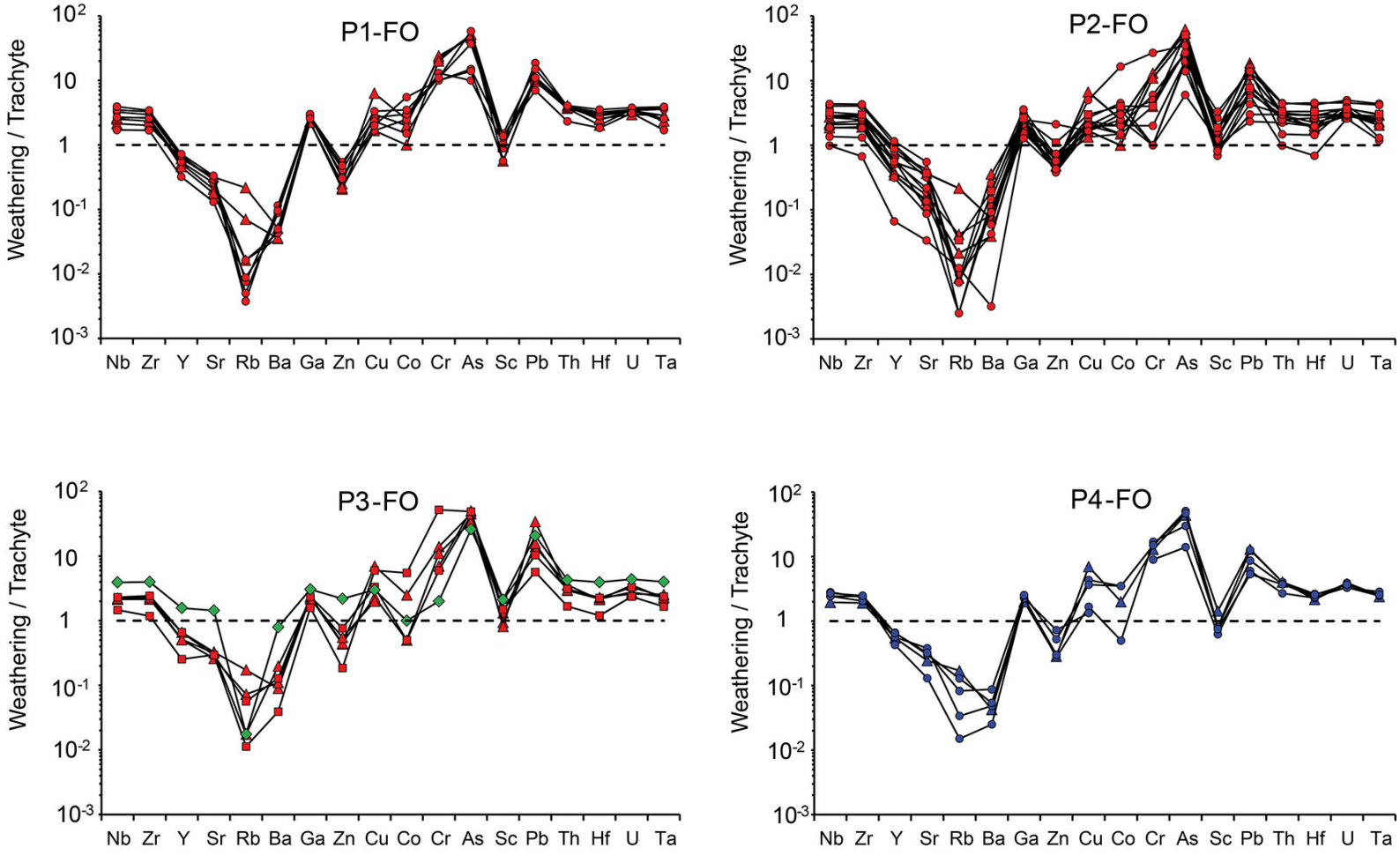
P1-FO
P2-FO
P3-FO
P4-FO
Weathering / Trachyte
10^2
10
1
10^{-1}
10^{-2}
10^{-3}
Nb Zr Y Sr Rb Ba Ga Zn Cu Co Cr As Sc Pb Th Hf U Ta
Plateau unit
Nodular bauxitic horizon (B11)
Massive bauxitic duricrust (B12)
Blocky bauxitic duricrust (B13)
Saprolite
Dowslope unit
Fine earthy horizon (B14)
Bauxitic pebbly duricrust (B15)

Fig. 8

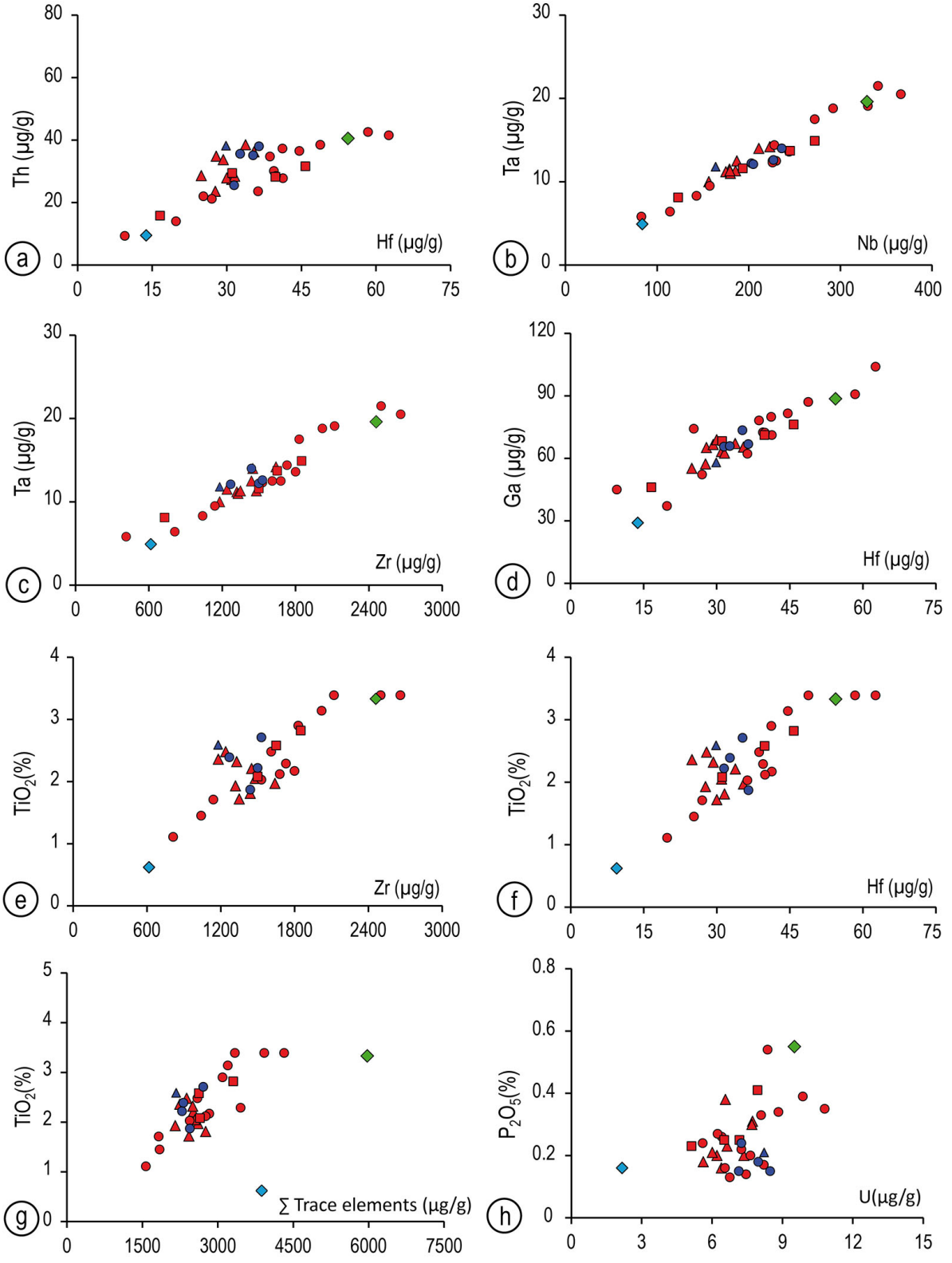

Plateau unit

- Nodular bauxitic horizon (B11)
- Massive bauxitic duricrust (B12)
- Blocky bauxitic duricrust (B13)

Dowslope unit

- Fine earthy horizon (B14)
- Bauxitic pebbly duricrust (B15)

- Saprolite (C)
- Trachyte

Fig. 9

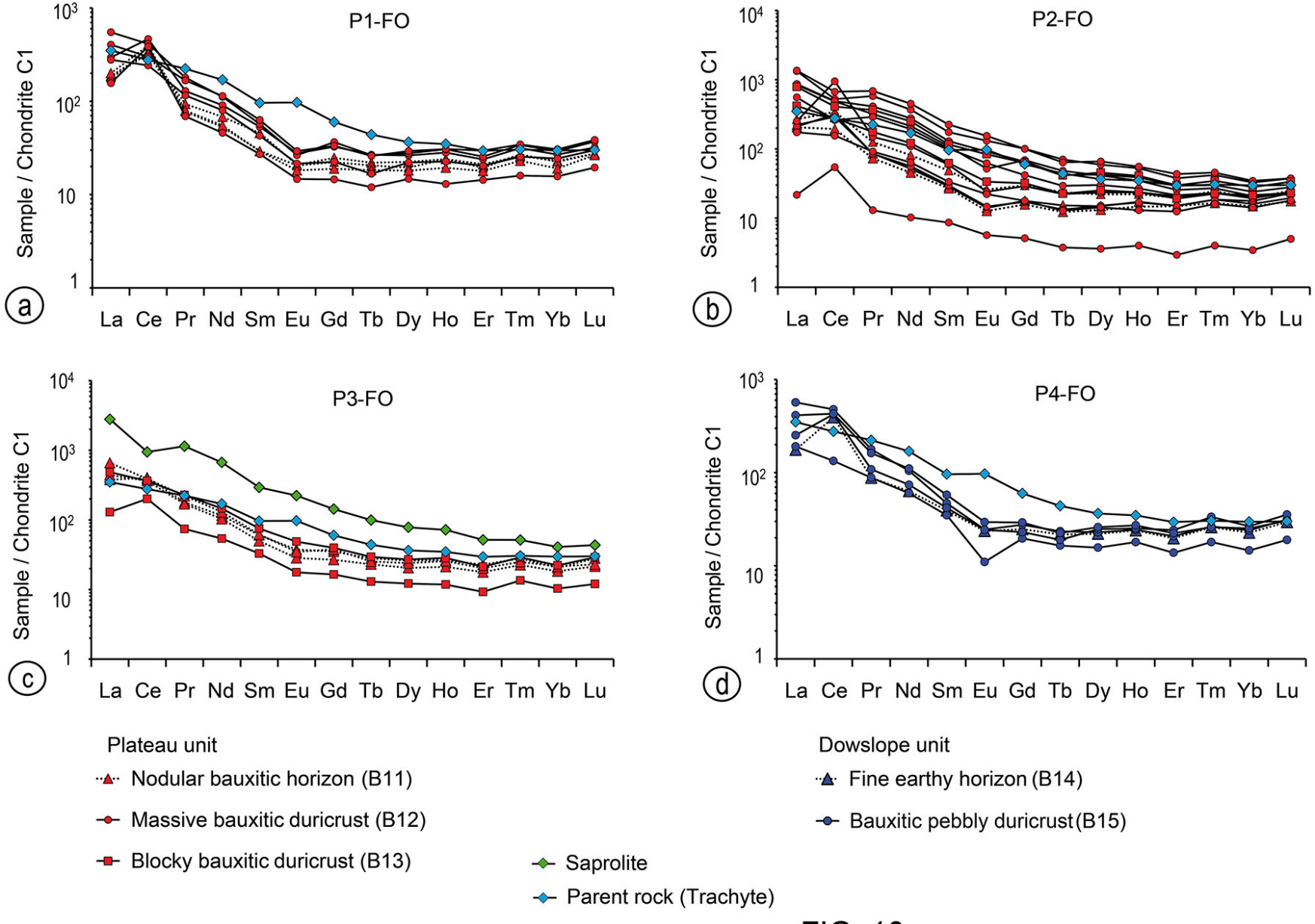
P1-FO
P2-FO
P3-FO
P4-FO
Sample / Chondrite C1
La Ce Pr Nd Sm Eu Gd Tb Dy Ho Er Tm Yb Lu
a
b
c
d
Plateau unit
Nodular bauxitic horizon (B11)
Massive bauxitic duricrust (B12)
Blocky bauxitic duricrust (B13)
Saprolite
Parent rock (Trachyte)
Dowslope unit
Fine earthy horizon (B14)
Bauxitic pebbly duricrust (B15)

FIG. 10

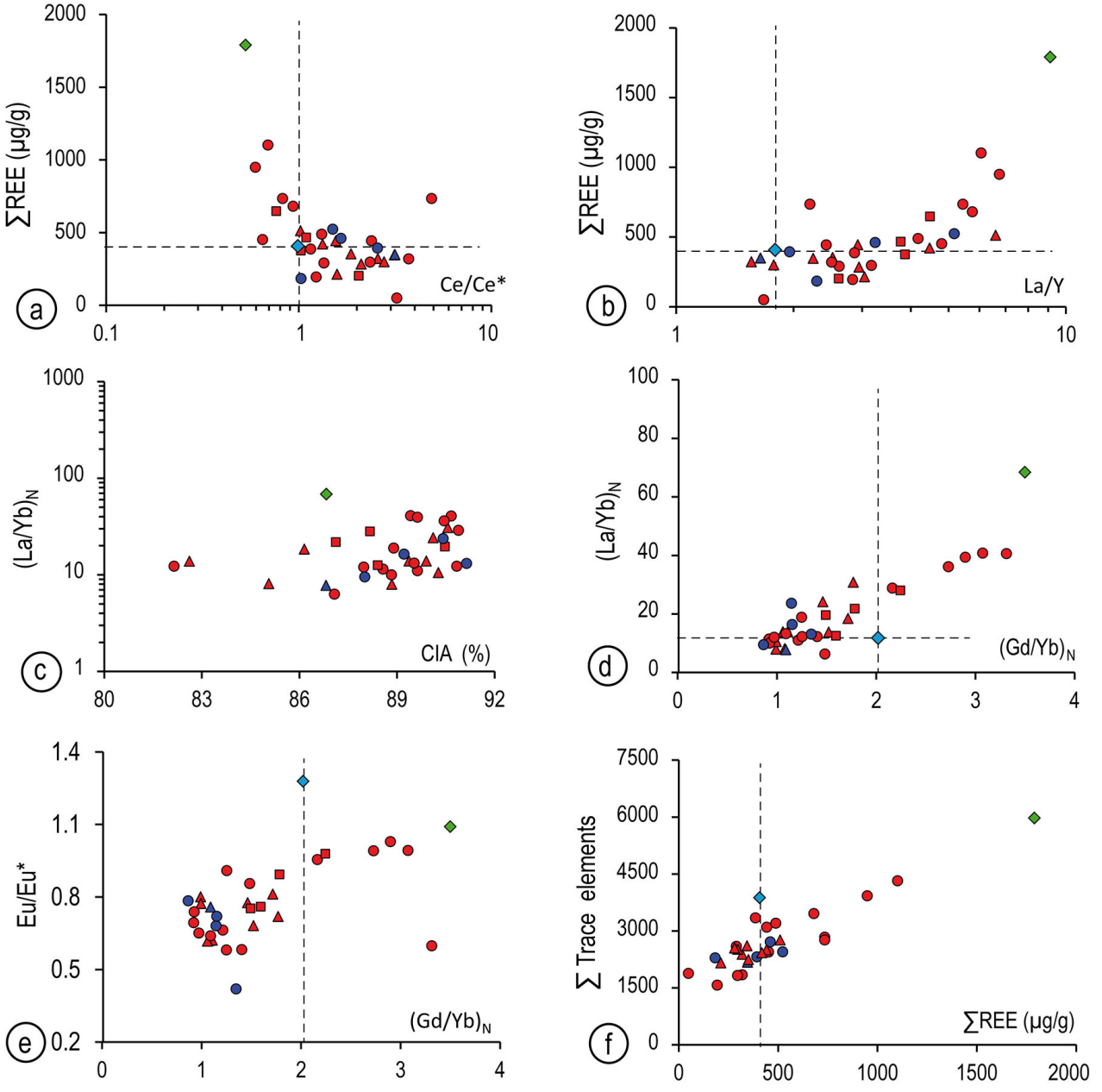
a
ΣREE (µg/g)
Ce/Ce*
b
La/Y
c
(La/Yb)N
CIA (%)
d
(Gd/Yb)N
e
Eu/Eu*
f
∑ Trace elements
ΣREE (µg/g)
Plateau unit
Nodular bauxitic horizon (B11)
Massive bauxitic duricrust (B12)
Blocky bauxitic duricrust (B13)
Saprolite (C)
Trachyte
Dowslope unit
Fine earthy horizon (B14)
Bauxitic pebbly duricrust (B15)

FIG. 11

	Horizon	Description	Depth (m)	Mineralogical composition (%)								
Plateau				**Ka**	**Bo**	**Gi**	**Go**	**An**	**He**	**Ma**	**Fl**	**Qz**
P1-FO-1.2	B11	Loose matrix	0.5	10		43	18	5	5	-		18
P1-FO-1.1	B11	Nodules	0.5	6	-	54	22	-	-	-		11
P1-FO-1	B11	Bauxitic blocks	0.5	-		70	20	-	5	-		
P1-FO-2	B12	Massive bauxite	2.8	-		67	21	-	9	-		
P1-FO-3.1	B12	Saprolitic bauxite	3.0	6		51	33	-	7	-		
P1-FO-3	B12	Massive bauxite	4.8	-		55	19	-	22	-	-	
P1-FO-4	B12	Massive bauxite	6.0	-		72	16	-	6	-		
P1-FO-4.1	B12	Saprolitic bauxite	6.0	-		54	33	-	5	5		
Upslope												
P2-FO-1.2	B11	Loose matrix	0.5	9		43	23	-	-	-		17
P2-FO-1.1	B11	Nodules	0.5	-		63	29	-	-	-		
P2-FO-1	B11	Bauxitic blocks	1.0			65	25	-	-	5		
P2-FO-2	B12	Massive bauxite	2.5	-		55	24	6	5	8	-	
P2-FO-3.1	B12	Saprolitic bauxite	4.0	-		68	29	-	-			
P2-FO-3	B12	Massive bauxite	4.5			55	30	6	7	-	-	
P2-FO-4	B12	Massive bauxite	6.0			59	26	-	7	-	-	
P2-FO-5.1	B12	Saprolitic bauxite	7.5	3		48	25	-	9	9		
P2-FO-5	B12	Massive bauxite	8.0			52	31	5	9	-	-	
P2-FO-6	B12	Massive bauxite	9.0	8		61	18	-	5	6		
P2-FO-7	B12	Massive bauxite	10.0	-		66	21	-	-	6	-	
P2-FO-7.1	B12	Dark brown domains	10.0			40	58	-		-		
P2-FO-8	B13	Bauxitic blocks	11.0	-		57	29	-	6	-		
P2-FO-8.1	B13	Nodules	11.0	16		49	22	-	7	-		
Hillside												
P3-FO-1.2	B11	Loose matrix	1.0	22		31	23	-	-	-		15
P3-FO-1.1	B11	Nodules	1.0	7	-	60	21	-	-	-		
P3-FO-1	B11	Bauxitic blocks	1.0	6	-	65	16	-	7	-		
P3-FO-2	B13	Loose matrix	5.0	56		23	8	5	-	-		-
P3-FO-2.1	B13	Nodules	5.0	10		49	19	7	13			
P3-FO-3	C	Saprolite	10.5	61		16	7	8	-	5	-	
Downslope												
P4-FO-1	B14	Loose fine earth	0.5	26		34	13	3	6	5		13
P4-FO-2	B15	Massive matrix	1.5	12		63	12	2	10	-		
P4-FO-2.1	B15	Coarse massive	1.7	7		71	16	3	-	-		
P4-FO-3	B15	Massive matrix	4.0	24		57	7	2	9	-		
P4-FO-4	B15	Massive matrix	5.0	28		54	9	3	-	-		

Table 1.

				Major oxides (%)												Weathering chemical indices			
	Horizon	Description	Depth (m)	SiO_2	Al_2O_3	Fe_2O_3	TiO_2	CaO	MgO	Na_2O	K_2O	MnO	P_2O_5	LOI	Total	CIA	IOL	MIA	Ki
Plateau			**d.l.**	0.01	0.01	0.01	0.01	0.01	0.01	0.01	0.01	0.01	0.01						
P1-FO-1.2	B11	Loose matrix	0.5	18.75	31.50	17.65	2.48	0.16	0.34	0.05	0.25	0.05	0.31	28.0	99.58	85.1	72.4	87.0	0.60
P1-FO-1.1	B11	Nodules	0.5	7.31	42.10	18.65	2.21	0.06	0.11	-	0.10	0.05	0.20	27.7	98.53	88.8	89.3	90.8	0.17
P1-FO-1	B11	Bauxitic blocks	0.5	2.34	48.40	18.45	1.97	0.03	0.02	-	0.03	0.04	0.16	28.2	99.68	90.3	96.6	92.0	0.05
P1-FO-2	B12	Massive bauxite	2.8	0.60	44.90	25.90	2.9	0.04	0.01	-	0.01	0.16	0.14	25.5	100.20	89.6	99.16	92.2	0.01
P1-FO-3.1	B12	Saprolitic bauxite	3.0	2.56	40.30	29.80	2.48	0.04	0.02	-	0.02	0.12	0.22	24.4	99.99	88.6	96.5	91.9	0.06
P1-FO-3	B12	Massive bauxite	4.8	0.80	41.60	29.60	3.14	0.04	0.03	-	0.01	0.18	0.2	23.9	99.54	88.9	98.9	92.0	0.02
P1-FO-4	B12	Massive bauxite	6.0	1.07	44.50	27.50	3.39	0.05	0.01	-	0.02	0.09	0.17	24.8	101.65	89.5	98.5	92.2	0.02
P1-FO-4.1	B12	Saprolitic bauxite	6.0	1.68	41.40	29.80	1.45	0.04	0.02	-	0.02	0.13	0.13	25.8	100.50	88.8	97.7	92.0	0.04
Upslope																			
P2-FO-1.2	B11	Loose matrix	0.5	19.25	26.70	17.55	2.36	0.28	0.47	0.08	0.28	0.08	0.38	31.3	98.77	82.6	69.7	84.8	0.72
P2-FO-1.1	B11	Nodules	0.5	3.92	44.00	22.70	2.05	0.05	0.07	-	0.05	0.15	0.23	27.6	100.86	89.4	94.5	91.5	0.09
P2-FO-1	B11	Bauxitic blocks	1.0	2.27	46.30	21.90	1.93	0.03	0.03	-	0.02	0.08	0.2	27.6	100.39	89.9	96.8	92.0	0.05
P2-FO-2	B12	Massive bauxite	2.5	1.97	50.70	14.25	2.29	0.02	0.01	-	0.03	0.06	0.33	28.9	98.68	90.7	97.1	91.9	0.04
P2-FO-3.1	B12	Saprolitic bauxite	4.0	2.29	38.10	34.50	1.71	0.08	0.01	-	0.02	0.06	0.34	23.9	101.03	88.0	96.9	92.0	0.06
P2-FO-3	B12	Massive bauxite	4.5	1.10	43.90	25.10	3.39	0.04	-	-	0.01	0.06	0.35	25.6	99.61	89.4	98.4	92.0	0.03
P2-FO-4	B12	Massive bauxite	6.0	0.73	49.20	20.50	2.17	0.02	-	-	0.01	0.05	0.26	27.4	100.39	90.5	99.0	92.3	0.01
P2-FO-5.1	B12	Saprolitic bauxite	7.5	2.16	35.00	32.80	8.00	0.02	0.64	-	0.01	0.12	0.24	20.9	99.92	87.1	96.9	89.2	0.06
P2-FO-5	B12	Massive bauxite	8.0	0.79	44.90	25.50	3.39	0.08	-	-	0.01	0.06	0.39	25.7	100.89	89.6	98.9	92.2	0.02
P2-FO-6	B12	Massive bauxite	9.0	1.80	51.50	17.45	2.12	0.02	-	-	0.01	0.09	0.16	27.2	100.37	90.8	97.5	92.4	0.03
P2-FO-7	B12	Massive bauxite	10.0	1.32	51.80	17.45	2.03	0.02	-	-	0.01	0.08	0.27	27.6	100.61	90.9	98.1	92.4	0.03
P2-FO-7.1	B12	Dark brown domains	10.0	1.66	23.90	52.70	1.11	0.01	-	-	0.01	0.17	0.54	20.4	100.53	82.2	97.9	91.7	0.07
P2-FO-8	B13	Bauxitic blocks	11.0	1.59	49.40	20.20	2.58	-	-	-	0.02	0.07	0.25	27	101.15	90.5	97.8	92.3	0.03
P2-FO-8.1	B13	Nodules	11.0	5.89	39.10	25.90	2.82	0.07	0.06	-	0.06	0.11	0.41	24.5	98.99	88.2	91.7	91.2	0.15
Hillside																			
P3-FO-1.2	B11	Loose matrix	1.0	19.45	33.60	17.00	2.32	0.10	0.21	0.01	0.19	0.06	0.30	26.3	99.58	86.2	72.2	88.2	0.58
P3-FO-1.1	B11	Nodules	1.0	4.61	47.60	17.35	1.72	0.03	0.03	-	0.04	0.12	0.21	27.3	99.05	90.1	93.4	91.7	0.10
P3-FO-1	B11	Bauxitic blocks	1.0	2.99	49.90	17.00	1.81	0.03	0.02	-	0.02	0.24	0.18	28.1	100.35	90.6	95.7	92.0	0.06
P3-FO-2	B13	Loose matrix	5.0	19.50	35.50	21.90	2.08	0.05	0.03	-	0.06	0.07	0.25	19.7	99.19	87.1	74.6	90.3	0.55
P3-FO-2.1	B13	Nodules	5.0	3.50	39.70	27.50	5.84	0.03	0.15	-	0.02	0.09	0.23	23.1	100.23	88.4	95.1	91.1	0.09
P3-FO-3	C	Saprolite	10.5	26.40	34.30	17.30	3.33	0.05	0.01	-	0.02	0.08	0.55	16.5	98.79	86.8	66.1	89.7	0.77
Downslope																			
P4-FO-1	B14	Loose fine earth	0.5	19.25	35.70	17.55	2.59	0.07	0.16	-	0.22	0.05	0.21	24.4	100.23	86.8	73.5	89.0	0.54
P4-FO-2	B15	Massive matrix	1.5	4.29	49.30	16.95	1.87	0.03	0.02	-	0.04	0.08	0.15	26.8	99.56	90.4	93.9	91.9	0.09
P4-FO-2.1	B15	Coarse massive pebbles	1.7	2.02	53.50	10.65	2.22	0.01	-	-	0.02	0.03	0.15	29.6	98.22	89.2	97.0	91.1	0.26
P4-FO-3	B15	Massive matrix	4.0	14.40	39.30	17.50	2.39	0.07	0.11	-	0.16	0.08	0.24	24.9	99.19	91.1	79.8	92.1	0.04
P4-FO-4	B15	Massive matrix	5.0	11.25	43.70	18.90	2.71	0.04	0.06	-	0.09	0.07	0.18	23.7	100.74	88.0	84.8	90.0	0.37
Parent rock			-	59.50	15.50	8.40	0.62	2.85	0.22	4.36	5.08	0.39	0.16	1.59	98.97	46.5	28.7	53.1	3.84

Table 2.

	Horizon	Description	Depth (m)	Trace elements (µg/g)																		
				Nb	Zr	Y	Sr	Rb	Ba	Ga	Zn	Cu	Ni	Co	Cr	V	As	Sc	Pb	Th	Hf	U	Ta
Plateau			**d.l.**	0.2	2	0.5	0.1	0.2	0.5	0.1	2	1	1	1	10	5	0.1	1	2	0.05	0.2	0.05	0.1
P1-FO-1.2	B11	Loose matrix	0.5	179	1240	28.6	38	17.3	134	65.2	47	19	24	5	220	211	5.1	16	29	35	28	7.7	12
P1-FO-1.1	B11	Nodules	0.5	211	1450	24.1	24.7	5.6	93.1	67.1	39	9	11	4	240	165	4.6	15	34	39	34	7.4	14
P1-FO-1	B11	Bauxitic blocks	0.5	223	1640	21.4	21.2	1.3	95.1	65.4	41	5	5	2	200	125	5.2	9	32	36	36	6.4	14
P1-FO-2	B12	Massive bauxite	2.8	272	1830	29.2	35.8	0.3	302	79.9	63	5	3	5	130	139	1	17	56	37	41	7.5	18
P1-FO-3 .1	B12	Saprolitic bauxite	3.0	226	1610	25.5	30.8	1.3	113	78.2	78	8	10	6	110	132	3.7	21	30	35	39	7.3	13
P1-FO-3	B12	Massive bauxite	4.8	292	2020	31.6	34.7	0.4	231	81.6	102	7	4	3	100	92	1.5	24	45	37	45	7.6	19
P1-FO-4	B12	Massive bauxite	6.0	330	2120	33.8	39.7	0.6	252	87.1	57	6	6	11	100	116	1.4	9	33	39	49	8.2	19
P1-FO-4. 1	B12	Saprolitic bauxite	6.0	143	1040	15.0	15.7	0.7	130.5	74.2	90	10	5	7	110	80	5.8	22	21	22	25	6.8	8.3
Upslope																							
P2-FO-1.2	B11	Loose matrix	0.5	156	1180	25.5	43.6	17	191	55.2	90	20	24	5	130	154	5.4	21	37	29	25	6.6	10
P2-FO-1.1	B11	Nodules	0.5	185	1480	18.1	20.3	3.3	221	63.2	122	7	4	3	130	107	6.2	25	56	27	31	6.6	11
P2-FO-1	B11	Bauxitic blocks	1.0	175	1320	16.2	16.7	1.7	103	57.3	121	5	3	2	110	88	4.6	21	26	24	28	6.2	11
P2-FO-2	B12	Massive bauxite	2.5	228	1730	35.1	50.9	0.7	939	72.5	108	4	2	3	40	49	2.9	28	51	30	40	8.1	14
P2-FO-3 .1	B12	Saprolitic bauxite	4.0	157	1140	16.0	16.1	0.8	111	52.2	76	6	7	4	60	73	2.7	16	7	21	27	8.8	9.5
P2-FO-3	B12	Massive bauxite	4.5	341	2500	47.4	43.5	0.6	482	90.8	87	7	5	4	20	45	2	42	48	43	58	11	22
P2-FO-4	B12	Massive bauxite	6.0	244	1800	38.2	38.8	0.2	380	71.2	72	5	5	5	10	25	1.9	11	19	28	41	6.4	14
P2-FO-5. 1	B12	Saprolitic bauxite	7.5	82.8	414	3.1	4.0	1.0	8.4	45	93	15	35	33	270	784	3.5	30	18	9.3	9.5	5.6	5.8
P2-FO-5	B12	Massive bauxite	8.0	366	2660	53.8	65.8	-	669	104	125	8	7	9	10	20	0.6	19	41	42	63	9.9	21
P2-FO-6	B12	Massive bauxite	9.0	230	1680	27.4	12.5	-	155	72.3	400	5	6	5	10	26	1.9	13	13	29	40	6.6	13
P2-FO-7	B12	Massive bauxite	10.0	226	1530	27.8	22.3	-	269	62.2	140	6	7	3	0	17	1.4	15	21	24	36	6.2	12
P2-FO-7. 1	B12	Dark brown domains	10.0	114	813	14.7	10.4	0.2	293	37.1	81	6	6	7	10	20	2	53	42	14	20	8.4	6.4
P2-FO-8	B13	Bauxitic blocks	11.0	245	1650	26.0	26	0.6	242	71.2	108	5	10	6	50	57	2.7	13	9	28	40	6.5	14
P2-FO-8.1	B13	Nodules	11.0	272	1850	42.2	44.1	2.7	518	76.2	207	9	10	8	40	51	5.1	30	23	32	46	7.9	15
Hillside																							
P3-FO-1.2	B11	Loose matrix	1.0	180	1330	31	39.2	13.8	236	66.6	82	21	27	5	140	162	4.5	21	42	34	29	7.7	11
P3-FO-1.1	B11	Nodules	1.0	179	1350	23.7	31.1	5.8	289	68.9	85	7	8	1	110	107	3.4	15	47	28	30	6	11
P3-FO-1	B11	Bauxitc blocks	1.0	187	1440	24	38	1.4	521	62.5	104	6	5	-	70	87	5	13	102	28	32	5.6	13
P3-FO-2	B13	Loose matrix	5.0	193	1500	30.9	35.1	4.5	338	68.3	145	10	12	1	60	81	4.3	34	31	29	31	7.2	12
P3-FO-2 .1	B13	Nodules	5.0	123	729	11.9	35.3	0.9	103	46.1	35	18	17	11	520	494	4.9	24	17	16	17	5.1	8.1
P3-FO-3	C	Saprolite	10.5	329	2460	73.6	172	1.4	2090	88.6	414	9	15	2	20	51	2.6	34	62	41	54	9.5	20
Downslope																							
P4-FO-1	B14	Loose fine earth	0.5	164	1180	25.7	29.2	13.6	112	58	54	21	28	4	130	180	4.4	23	39	38	30	8.2	12
P4-FO-2	B15	Massive matrix	1.5	236	1440	26.4	45.4	2.7	127.5	66.8	52	5	7	1	170	96	3	13	38	38	37	7.1	14
P4-FO-2.1	B15	Coarse massive pebbles	1.7	203	1500	20	15.6	1.2	65.8	65.6	137	4	2	-	90	61	1.4	10	16	35	35	8	13
P4-FO-3	B15	Massive matrix	4.0	205	1270	31	36.1	10.3	142	65.9	57	13	24	7	150	158	5.1	13	18	26	32	8.5	12
P4-FO-4	B15	Massive matrix	5.0	227	1530	30.6	38.4	6.6	230	73.5	99	11	18	7	150	148	4.7	12	26	36	33	7.3	12
Parent rock			-	83	617	46.8	119.5	79.8	2630	29	189	3	-	2	10	-	0.1	16	3	9.5	14	22	4,9

Table 3.

	SiO_2	Al_2O_3	Fe_2O_3	TiO_2	CaO	MgO	Na_2O	K_2O	MnO	P_2O_5
Nb	-0.11	**0.36**	-0.20	**0.86**	-0.10	-0.50	-0.20	-0.28	-0.13	0.13
Zr	-0.06	**0.35**	-0.24	**0.83**	-0.07	-0.54	-0.18	-0.27	-0.14	0.19
Y	**0.34**	**0.02**	-0.28	**0.75**	0.11	-0.33	-0.03	-0.01	-0.22	0.49
Sr	**0.49**	-0.14	-0.25	**0.55**	0.15	-0.13	0.06	0.03	-0.10	0.53
Rb	**0.74**	-0.53	-0.35	0.00	**0.78**	**0.57**	**0.71**	**0.99**	-0.28	0.08
Ba	0.32	-0.06	-0.14	**0.40**	-0.04	-0.25	-0.10	-0.18	0.02	0.62
Ga	-0.04	**0.34**	-0.25	**0.80**	-0.05	-0.43	-0.18	-0.21	-0.11	0.00
Zn	0.22	0.07	-0.17	0.18	-0.12	-0.20	-0.12	-0.23	0.02	0.32
Cu	**0.66**	-0.67	-0.08	0.12	**0.64**	**0.73**	**0.54**	**0.80**	-0.18	0.14
Ni	**0.64**	-0.61	-0.08	0.14	**0.47**	**0.81**	**0.41**	**0.69**	-0.21	0.15
Co	-0.18	-0.27	**0.42**	**0.37**	-0.03	**0.66**	-0.01	-0.07	0.08	0.05
Cr	0.06	-0.17	-0.01	-0.09	0.11	**0.49**	0.14	0.23	-0.05	-0.33
V	0.04	-0.28	0.16	0.07	0.05	**0.78**	0.09	0.12	0.06	-0.16
As	**0.42**	-0.32	-0.17	-0.36	0.35	0.37	0.29	0.51	0.04	-0.13
Sc	0,20	-0,60	**0,56**	-0,02	-0,03	0,08	-0,05	-0,09	0,21	0,65
Pb	0.12	-0.01	-0.11	0.11	0.05	-0.12	0.01	0.00	**0.57**	0.14
Th	0.27	0.15	-0.43	**0.79**	0.20	-0.30	0.03	-0.29	-0.25	-0.04
Hf	-0.10	**0.36**	-0.20	**0.83**	-0.09	-0.55	-0.21	-0.26	-0.14	0.19
U	0.15	-0.18	0.12	**0.58**	0.10	-0.28	-0.07	0.01	-0.30	**0.50**
Ta	-0.07	**0.34**	-0.24	**0.87**	-0.06	-0.45	-0.17	-022	-0.10	**0.66**
La	**0.25**	0.04	-0.17	0.05	-0.05	-0.29	-0.13	-0.22	-0.08	**0.57**
Ce	**0.24**	0.16	-0.32	-0.16	0.04	-0.32	-0.06	-0.05	-0.11	0.21
Pr	**0.24**	0.02	-0.15	0.06	-0.03	-0.28	-0.11	-0.21	-0.14	**0.60**
Nd	**0.21**	0.04	-0.14	0.06	-0.03	-0.29	-0.12	-0.22	-0.16	**0.60**
Sm	**0.21**	0.04	-0.15	0.07	0.00	-0.29	-0.09	-0.20	-0.18	**0.60**
Eu	**0.24**	-0.02	-0.10	0.09	0.00	-0.25	-0.10	-0.19	-0.17	**0.62**
Gd	**0.21**	0.04	-0.17	0.05	0.01	-0.29	-0.08	-0.17	-0.16	**0.59**
Tb	**0.26**	0.03	-0.22	0.03	0.03	-0.28	-0.06	-0.13	-0.19	**0.57**
Dy	**0.20**	0.06	-0.18	0.00	0.04	-0.33	-0.08	-0.13	-0.20	**0.55**
Ho	**0.26**	0.06	-0.23	-0.03	0.06	-0.34	-0.07	-0.09	-0.19	**0.50**
Er	**0.25**	0.06	-0.22	-0.09	0.11	-0.37	-0.04	-0.05	-0.18	**0.45**
Tm	**0.31**	0.00	-0.23	-0.13	0.16	-0.37	-0.03	0.04	-0.15	**0.37**
Yb	**0.26**	0.04	-0.20	-0.18	0.13	-0.42	-0.05	0.02	-0.10	**0.29**
Lu	**0.31**	-0.02	-0.18	-0.23	0.18	-0.39	-0.02	0.12	-0.14	**0.21**

Table 4.

	Horizon	Depth (m)	REE (µg/g)																					
			La	Ce	Pr	Nd	Sm	Eu	Gd	Tb	Dy	Ho	Er	Tm	Yb	Lu	∑REE	∑LREE	∑HREE	La/Y	Ce/Ce*	Eu/Eu*	$(La/Yb)_N$	$(Gd/Yb)_N$
Plateau		d.l.	0.5	0.5	0.03	0.1	0.03	0.03	0.05	0.01	0.05	0.01	0.03	0.01	0.03	0.01								
P1-FO-1.2	B11	0.5	44.6	207.0	8.4	31.3	6.9	1.3	5.0	0.9	5.6	1.2	3.4	0.5	3.7	0.6	320	304	16	1.56	2.58	0.62	8.1	1.1
P1-FO-1.1	B11	0.5	42.9	199.0	7.0	24.3	4.4	1.2	4.5	0.8	4.9	1.2	3.1	0.5	3.6	0.6	298	283	15	1.78	2.77	0.80	8.0	1.0
P1-FO-1	B11	0.5	48.1	242.0	7.2	25.3	4.4	1.1	3.8	0.7	4.5	1.0	2.9	0.5	3.1	0.5	345	332	13	2.25	3.14	0.77	10.5	1.0
P1-FO-2	B12	2.8	70.9	284.0	11.6	41.7	8.0	1.7	6.5	1.1	6.6	1.4	3.8	0.6	4.3	0.6	443	424	18	2.43	2.39	0.66	11.0	1.2
P1-FO-3.1	B12	3.0	66.8	148.0	10.4	36.8	6.4	1.3	4.5	0.7	5.5	1.1	3.3	0.5	3.9	0.6	290	274	16	2.62	1.35	0.69	11.4	0.9
P1-FO-3	B12	4.8	132.0	252.0	16.2	51.3	8.6	1.6	7.3	1.1	6.9	1.5	4.1	0.7	4.7	0.7	489	469	20	4.18	1.31	0.58	18.8	1.3
P1-FO-4	B12	6.0	97.0	183.0	15.1	52.4	9.5	1.8	6.7	1.0	7.3	1.5	4.7	0.7	4.9	0.8	386	365	21	2.87	1.15	0.64	13.2	1.1
P1-FO-4.1	B12	6.0	37.6	236.0	6.2	21.1	4.1	0.9	2.9	0.5	3.7	0.7	2.3	0.3	2.5	0.4	319	309	10	2.51	3.72	0.74	10.0	0.9
Upslope																								
P2-FO-1.2	B11	0.5	64.3	209.0	11.3	37.3	7.3	1.6	5.9	0.9	5.5	1.1	3.2	0.5	3.1	0.5	351	337	15	2.52	1.87	0.68	13.8	1.5
P2-FO-1.1	B11	0.5	53.3	177.5	7.7	23.8	4.3	0.8	3.6	0.6	3.7	0.9	2.4	0.4	2.6	0.4	282	271	11	2.94	2.11	0.62	13.9	1.1
P2-FO-1	B11	1.0	49.3	118.0	6.6	20.8	4.0	0.8	3.1	0.5	3.3	0.7	2.4	0.3	2.4	0.4	213	203	10	3.04	1.58	0.62	13.9	1.1
P2-FO-2	B12	2.5	202.0	296.0	28.8	98.0	16.3	3.1	13.8	1.9	10.3	1.7	4.1	0.5	3.3	0.4	680	658	22	5.75	0.94	0.60	40.6	3.3
P2-FO-3.1	B12	4.0	50.7	192.0	7.7	25.7	4.5	0.9	3.4	0.5	3.8	0.8	2.4	0.4	2.8	0.5	296	285	11	3.17	2.35	0.65	12.0	1.0
P2-FO-3	B12	4.5	320.0	320.0	52.3	169.5	26.2	7.9	20.1	2.8	14.8	2.6	6.0	0.8	5.2	0.8	949	916	33	6.75	0.60	0.99	40.8	3.1
P2-FO-4	B12	6.0	208.0	300.0	37.0	127.5	19.4	5.5	13.1	1.7	10.7	1.9	4.7	0.6	3.8	0.6	734	710	24	5.45	0.82	0.99	36.1	2.7
P2-FO-5.1	B12	7.5	5.2	33.1	1.2	4.7	1.3	0.3	1.0	0.2	0.9	0.2	0.5	0.1	0.6	0.1	49	47	2	1.68	3.23	0.86	6.3	1.5
P2-FO-5	B12	8.0	326.0	408.0	61.9	207.0	33.7	9.3	20.0	2.6	16.5	2.8	6.9	0.9	5.5	0.8	1102	1066	36	6.06	0.69	1.03	39.4	2.9
P2-FO-6	B12	9.0	60.4	579.0	13.5	50.1	8.8	1.4	5.8	0.9	5.9	1.2	3.3	0.5	3.3	0.5	734	719	15	2.20	4.89	0.58	12.2	1.4
P2-FO-7	B12	10.0	133.5	159.0	26.1	88.7	15.2	3.7	8.4	1.2	7.5	1.3	3.4	0.5	3.1	0.5	452	435	17	4.80	0.65	0.95	28.8	2.2
P2-FO-7.1	B12	10.0	41.7	94.9	8.2	29.3	5.0	1.3	3.6	0.5	3.6	0.7	2.0	0.3	2.3	0.4	194	184	10	2.84	1.23	0.91	12.2	1.3
P2-FO-8	B13	11.0	100.5	170.0	15.9	55.5	9.3	2.0	6.4	0.9	6.3	1.2	3.1	0.5	3.4	0.5	375	360	16	3.87	1.03	0.75	19.6	1.5
P2-FO-8.1	B13	11.0	189.0	250.0	32.9	115.0	17.4	5.0	12.6	1.7	11.4	2.0	4.8	0.7	4.5	0.7	648	622	26	4.48	0.76	0.98	28.1	2.2
Hillside																								
P3-FO-1.2	B11	1.0	90.7	247.0	16.1	53.2	9.1	2.3	7.0	1.1	6.5	1.3	3.6	0.6	3.3	0.6	442	425	17	2.93	1.56	0.81	18.4	1.7
P3-FO-1.1	B11	1.0	106.0	222.0	15.3	47.5	7.5	1.7	5.4	0.9	5.1	1.1	2.8	0.5	2.9	0.4	419	405	14	4.47	1.33	0.78	24.1	1.5
P3-FO-1	B11	1.0	158.5	238.0	19.9	59.8	9.3	2.1	7.6	1.0	6.0	1.3	3.2	0.5	3.4	0.5	511	495	16	6.6	1.02	0.72	30.8	1.8
P3-FO-2	B13	5.0	116.5	222.0	20.5	67.2	11.3	2.9	7.9	1.2	6.8	1.4	3.4	0.6	3.6	0.6	466	448	17	3.77	1.09	0.89	21.8	1.8
P3-FO-2.1	B13	5.0	31.1	122.5	6.7	24.8	4.9	1.1	3.3	0.5	3.0	0.6	1.5	0.3	1.7	0.2	202	194	8	2.61	2.05	0.76	12.6	1.6
P3-FO-3	C	10.5	671.0	578.0	103.0	308.0	44.0	13.4	28.6	4.0	19.6	3.6	8.3	1.0	6.5	0.9	1790	1746	44	9.12	0.53	1.09	68.4	3.5
Downslope																								
P4-FO-1	B14	0.5	42.3	240.0	7.9	29.2	5.9	1.4	5.0	0.9	5.5	1.2	3.2	0.5	3.6	0.6	347	332	15	1.65	3.16	0.76	7.8	1.1
P4-FO-2	B15	1.5	136.5	292.0	16.1	48.2	7.0	1.5	5.5	0.9	5.7	1.2	3.3	0.5	3.9	0.6	523	507	16	5.17	1.50	0.68	23.6	1.1
P4-FO-2.1	B15	1.7	45.9	81.6	8.0	27.7	5.2	0.7	3.9	0.7	3.9	0.9	2.2	0.4	2.3	0.4	184	173	11	1.50	1.03	0.42	13.1	1.3
P4-FO-3	B15	4.0	60.6	259.0	9.8	34.1	6.3	1.5	4.6	0.8	6.2	1.3	3.9	0.7	4.3	0.7	394	376	18	3.03	2.56	0.78	9.5	0.9
P4-FO-4	B15	5.0	99.2	262.0	14.6	50.9	8.7	1.8	5.8	0.9	6.5	1.4	3.6	0.5	4.0	0.6	460	443	18	3.2	1.66	0.72	16.4	1.2
Parent rock		-	84.0	169.0	20.1	78.1	14.5	5.8	12.0	1.8	9.1	1.7	4.7	0.6	4.8	0.6	407	383	23	1.79	0.99	1.28	11.8	2.0

Table 5.